Molecular basis of uracil/H^+ symport mechanism operated by the FurE/NCS1 transporter

Iliana Zantza[1], Georgia F. Papadaki[2,#] Stefano Raniolo[3,#], Yiannis Pyrris[2], Vittorio Limongelli[3,4*], George Diallinas[2,5*], Emmanuel Mikros[1,6*]

*co-corresponding authors
[#]equal contribution

[1]Department of Pharmacy, National and Kapodistrian University of Athens, Panepistimiopolis, Athens, 15771, Greece.

[2]Department of Biology, National and Kapodistrian University of Athens, Panepistimiopolis, Athens, 15784, Greece.

[3]Faculty of Biomedical Sciences, Euler Institute, Università della Svizzera italiana (USI), Lugano, 6900, Switzerland

[4]Department of Pharmacy, University of Naples "Federico II", Naples, 80131, Italy

[5]Institute of Molecular Biology and Biotechnology, Foundation for Research and Technology, Heraklion, 70013, Greece.

[6]Athena Research and Innovation Center in Information Communication & Knowledge Technologies, Marousi, 15125, Greece

Abstract

Transporters mediate the uptake or efflux of solutes, metabolites and drugs across the cell membrane. The FurE symporter of uracil-allantoin-uric acid/H^+ of *Aspergillus nidulans* has been used as a model eukaryotic transporter to address structure-function relationships and the mechanism of transport in the NCS1/APC family of transporters. Extensive genetic, functional and cellular studies, as well as homology modeling based on a prokaryotic transporter with a similar fold (Mhp1) have provided important information on specific structural elements of FurE. However, the exact mechanism by which substrates and proton or other cations are translocated by FurE or transporters with a similar fold remains elusive. In this study, we reveal the binding mode, translocation and release pathway of uracil/H^+ from the extracellular space to the cytoplasm, using novel metadynamics calculations and rationally designed mutational analysis. In particular, Metadynamics Free Energy Surface maps provide the relative order of internalization of uracil and proton, permitting also selection of intermediate conformational states related to transport cycle. Funnel Metadynamics allow the sampling of specific interactions of both uracil and proton with residues during their internalization, generating a holistic model of the transport events in conjunction with experimental mutation studies. Our work not only complements and extends the existing knowledge on FurE same-fold transporters, but also challenges the so-called rocking bundle mechanism associated with biomedically interesting members of the APC superfamily of transporters.

Keywords: Nucleobase/H^+ symporter, Metadynamics, FurE, uracil

Introduction

Secondary active transporters are transmembrane proteins that play a key role in transporting nutrients inside the cells. They select and translocate their substrates using the energy provided by the electrochemical gradient of the membrane, via a mechanism that involves the symport or exchange antiport of Na^+/H^+ cations with other solutes. Structural studies revealed that although secondary active transporters may be structurally, functionally or evolutionary distinct, they share common folds, which are related to specific protein conformational changes associated with the solute transport cycle. The general model for the transport mechanism is known as the "alternating-access model", where the transporter accepts or releases the substrate at one side of the cell membrane by changing conformations from an *outward-open* (OO) state facing the extracellular environment to an *inward-open* (IO) state facing the cytosol.[1–5] Depending on the folding and specific conformational rearrangements of the transporter, three major mechanisms have been proposed, namely the rocker-switch, the rocking-bundle and the sliding-elevator.[5–9] Important structural and functional information about the rocking-bundle mechanism, which characterizes one of the largest transporter families, the so-called Amino Acid-Polyamine-Organocation (APC) Family (TC# 2.A.3), rise from seminal studies on the bacterial transporter LeuT specific for leucine and alanine.[3,5,10] LeuT adopts the 5+5 helical inverted repeat (5HIRT), formed by the first 10 transmembrane helices whose structural elements and conformational changes determine substrate recognition and transport. In total, LeuT and similar transporters possess twelve transmembrane α-helical segments (TMSs), however the role of TMS11 and TMS12 is not yet clarified. The rocking-bundle model assumes that translocation of the substrate following the OO-to-IO conformational change is facilitated by the relative motion between two motifs, the so-called *hash*/scaffold domain (TMS3, TMS4, TMS8, TMS9) and the *bundle*/core domain (TMS1, TMS2, TMS6, TMS7), with TMS5 and TMS10 functioning as gates. It has been suggested that substrate binding in the OO conformation is assisted by the simultaneous binding of a positive charge (Na^+ or H^+) inducing the conformational change of the protein towards the IO conformation. This paradigm of substrate translocation mechanism has been supported by studies on the eukaryotic dopamine (DAT)[11] and serotonin (SERT)[12] transporters (neurotransmitter/sodium symporter family-NSS), and a number of prokaryotic transporters, including the MhsT transporter specific for hydrophobic L-amino acids (NSS family),[13] the sodium-galactose symporter vSGLT (sodium-solute symporter-SSS family),[14] the sodium-betaine symporter BetP[15] and CaiT[16] (betaine/choline/carnitine transporter-BCCT family), the AdiC[17] and ApcT[18] (amino acid/polyamine/organocation-APC family) and, finally, the bacterial benzyl-hydantoin/Na+ symporter Mhp1[19–22] (nucleobase cation symporter 1 or NCS1 family). Although all these proteins share the same fold, topological differences have been found during the transition from the OO to the IO state. LeuT and MhsT crystal structures suggest that the bundle/core domain (TMS1, TMS2, TMS6, TMS7), undergoes significant conformational changes during the OO/IO transition pivoting around the hash/scaffold motif, while there are two additional rearrangements functioning as opening-closing gates. Specifically, in LeuT the displacement of TMS1b, TMS6a acts as an extracellular gate, along with a 45-degree kink of the TMS1a followed by a local unwinding of TMS5 which functions as the intracellular one. In contrast, the Mhp1 transporter transits from the outward- to the inward-state by pivoting the hash motif around the bundle domain, which also promotes TMS10 to move towards TMS1b and TMS6a to pack the substrate in the occluded conformation. Moreover, TMS5 bending opens the inward facing cavity, as opposed to LeuT's TMS1a.

Several fungal members of the NCS1 transporter family, related to the APC superfamily, have been extensively studied by Diallinas and co-workers, unveiling important information about regulation of expression, subcellular trafficking and turnover, transport kinetics, and substrate specificity.[23–29] Transporters of this family function as high- or low-

affinity H^+ symporters selective for uracil, cytosine, allantoin, uridine, thiamine or nicotinamide riboside and secondarily for uric acid and xanthine.[23,24,30] NCS1 transporters are present mostly in bacteria and fungi, thus characterizing the relative transport mechanism in atomic detail will not only improve our understanding of the complex machinery of LeuT-like transporters, but might also provide valuable insight into developing novel antibacterial or antifungal drugs. In previous studies, we have used the Mhp1 transporter, as a structural template for modeling specific members of the NCS1 family and assessed the results with functional data obtained by extensive mutational analyses. From these studies, we defined the putative substrate binding sites in several NCS1 members of the fungus *Aspergillus*, namely the FcyB purine-cytosine transporter,[25] the FurA allantoin transporter,[26] the FurD uracil transporter,[26] and the FurE uracil-allantoin-uric acid transporter.[26,28] Recently, we have focused on the role of the cytosolic N-and C-terminal segments on FurE, showing their crucial role in regulating endocytic turnover, transport kinetics, and affecting surprisingly substrate specificity.[28,29] Related to the latter finding, a homology model suggested that the N-terminus of FurE regulates substrate selectivity by interacting dynamically and in a pH-dependent manner with specific intracellular loops.[28,29] Interestingly, a similar role of the N-terminal region has been also found in eukaryotic LeuT-like transporters, such as the *Drosophila melanogaster* DAT (dDAT) and human SERT (hSERT).[31]

In the present study, we sought to describe at atomistic resolution the functional conformational changes operated by FurE from the OO to the IO state. We investigated the translocation pathway through the intermediate occluded state (Occ) and elucidated the role and the order of the internalization of both uracil as substrate and H^+ cation (in the form of hydronium H_3O^+). To this end, we employed advanced computational methods and additional mutational analyses, rationally designed to assess the *in silico* results. Starting from the three conformational states resolved for Mhp1, we constructed the corresponding FurE homology models and performed metadynamics calculations,[32] a powerful enhanced-sampling technique able to reproduce slow-rate biological processes at an affordable computational cost. In particular, the binding sites and translocation pathways of both H_3O^+ and uracil substrate have been characterized through funnel-metadynamics (FM),[33] a variant of metadynamics purposely developed for ligand binding studies. Overall, we were able to characterize the large-scale conformational changes of the transporter from the OO to the IO state, including the transport of both the substrate and H_3O^+, thus providing a comprehensive new picture of the functional mechanism of FurE and NCS1 transporters in general.

Results

FurE 3D structure

The FurE structure in three different conformational states, Outward Open (OO), Occluded (Occ) and Inward Open (IO), was built through homology modeling and Targeted Molecular Dynamics calculations, using the available Mhp1 crystal structures with PDB IDs 2JLN, 4D1B, and 2X79, respectively.[20–22] The sequence identity of FurE and Mhp1 is 23.9%, excluding the cytosolic terminal regions that are highly variable. The length of TMS helices and loops of FurE have no major difference compared to those of Mhp1. All structures were subjected to 50 ns of MD simulations for structure relaxation and equilibration. The obtained three FurE structures are shown in **Figure 1**.

Upon a close visual inspection of the structures, it emerges that the majority of charged residues are arginines and lysines positioned on the outer surface FurE and facing the cytoplasmic environment, with few exceptions that are important for the structure and function of the transporter. For example, R123 (TMS3) can form a salt bridge with D261 (TMS6), mimicking the interaction observed in Mhp1 between K110 (TMS3) and D229 (TMS6). In

Mhp1, the two residues interact at 3.87 Å in the IO conformer, while they are at more than 5 Å in the Occ and OO conformers. At variance with Mhp1, in FurE this interaction is formed in all three conformers due to the bigger size of arginine compared to lysine, with the distance between D261 carboxylate and R123 guanidinium being 3.0 Å in OO, 2.85 Å in Occ, and 3.5 Å in IO (**Figure S2A**). In very close proximity, the D348 (TMS9) carboxylate points towards the D261-R123 interaction, but since its pKa is calculated to be 8, it was considered as neutral and thus does not seem to participate in the D261-R123 charge neutralization.

Another important interaction is that formed between E51 at the edge of TMS1a and K199 positioned in the middle of TMS5. The side chains of both residues are rather flexible, and their interaction might not be stable, with a distance ranging from 2.7 Å in Occ to 3.9 Å in OO (**Figure S2B**). In IO, K199 side chain has been completely reoriented pointing to the lipid interface of the protein (**Figure S2B**). Interestingly, in both OO and Occ cases, the K199 side-chain amino group is situated in the position of the co-crystallized Na^+ cation in the Occ conformation of Mhp1 and very close to that of the second Na^+ (Na2) present in the equivalent structure of LeuT (**Figure S2C**). It is worth noting that an additional K252 (TMS6), which has been shown to affect substrate specificity,[28] might also form a second salt bridge with E51 in the OO conformation (**Figure S2B**). In Mhp1, this residue corresponds to W220, which is considered as one of the main residues participating in substrate recognition and translocation. In the other two conformers, no interaction between K252 and E51 is observed. Finally, the N-terminal D28 interaction with K188 (TMS5), reported by Papadaki *et al*., is present only in the OO structure.[29] In Occ, D28 forms a stable salt bridge with R264, while in IO the distance between D28 carboxylate oxygens and R264 guanidinium nitrogen atoms is around 5 Å (**Figure S2A**).

Apart from the aforementioned, "static" salt bridges, other interactions possibly involved in the function of the outer gate can be related to the OO-to-Occ conformational transition. For example, the Q59 side chain (TMS1b) could approach S386 (TMS10) side chain (**Figure S2D**) as well as S43 (TMS1) and R193 (TMS5), at least in the OO structure, while in the other conformers R193 is oriented towards the surrounding lipids. A similar gating network involving TMS1, TMS5 or TMS10 have also been proposed in LeuT and Mph1.

Overall, in the generated structures of FurE the relative orientation of the TMSs in OO, Occ and IO conformations follows that of the Mhp1 structural templates, however small discrepancies arise. When the structures are aligned based on the "bundle" motif Cα atoms, we observe that FurE OO and Occ conformations are in quite good agreement with the Mhp1 templates, whereas in the IO conformer TMS4 and TMS9 are not optimally aligned with the corresponding template helices (**Figure S3**). Considering that the detected TMS shift is observed after only 50 ns of MD simulation relaxation, it implies a relative flexibility of TMS4 and TMS9.

Mutational analysis confirms the crucial role of specific residues in FurE transport function

The FurE structural models highlight two salt bridges, namely R123-D261 and E51-K199, and a polar interaction between Q59 and S384 or S386 as important in stabilizing the diverse states and supposed to be crucial in the conformational transition. Additional residues found to be related to putative conformational changes and the assumed substrate pathway were W39, T63, S64, R193, F196, R264, N347 and F385. In order to further support the possible functional role of these residues hypothesized from the described models, we performed a rational mutational analysis of the aforementioned residues in FurE. Using a standard directed mutagenesis protocol, the following Ala substitutions mutations were constructed: **W39A, E51A, Q59A, T63A, S64A, R123A, R193A, F196A, K199A, D261A, R264A, N347A, S384A, F385A and S386A.** Other residues predicted from the FurE structure to be important for transport activity,

such as the interaction of D28 with K188, and the critical role of K252 in substrate binding and specificity, have been previously supported by analogous Ala substitutions.[29] All mutated versions of FurE were introduced by genetic transformation in the *A. nidulans* Δ7 strain, genetically lacking all major nucleobase-related transporters, The mutant versions of FurE, as well as a wild-type FurE control, were expressed *via* the strong *gpdA* promoter, fused in frame with the gfp gene at their C-terminus, as previously described.[28,29] Several selected transformants for each mutation were purified and tested for growth in media containing purines as nitrogen sources or 5-fluorouracil (5-FU, a uracil toxic analogue). Transformants expressing a specific mutation showed, as expected, similar growth phenotypes.

Figure 2A (upper left panel) summarizes the growth phenotypes tested for all engineered mutants and control strains. As expected, the positive control strain expressing wild-type FurE grows on allantoin and uric acid and is sensitive to 5-FU, whereas the negative control strain not expressing FurE (see Materials and methods) shows a N starvation growth phenotype and is resistant to 5-FU. Ala substitutions in residues predicted to form the two major salt bridges (R123-D261 and E51-K199) scored as loss-of-function mutations as reflected in abolishment or dramatic reduction of growth on allantoin or uric acid, and relatively increased resistance to 5-FU, mostly evident in R123A and D261A. Similar dramatic loss of FurE transport activity was obtained in R264A and F385A mutants, while Q59A and S386A FurE versions seemed to have lost their transport activity for uric acid or 5-FU, but conserved some capacity for allantoin transport. Thus, mutational analyses confirmed the essential functional role of the interactions between R123-D261, E51-K199 and Q59-S385-S386, as well as the essentiality of R264 via its predicted interaction with N-terminal D28, as supported by mutating D28.[29] Our analysis also revealed an important role of W39, as its substitution led to loss of FurE-mediated uric acid and allantoin transporter, although 5-FU transport seemed to be conserved, since sensitivity to this drug is retained. Our results further showed that Ala substitution of T63, S64, R193 or F196 have moderate negative effects on FurE apparent activity, reflected in reduction of growth on uric acid and some increase in 5-FU resistance (e.g. F196A). Finally, residues N347 and S384 proved non-essential for FurE activity.

Epifluorescence microscopic analysis, shown in the right panel of **Figure 2A** confirmed that mutational disruption of the major interactions tested (R123-D261, E51-K199 and Q59-F385-S386) did not affect the normal PM localization and stability of FurE, which further confirms that the associated growth defects in specific mutants reflect defects in FurE transport activity *per se*, rather than an effect on protein folding or subcellular trafficking. This conclusion was further strengthened by direct transport assays, which showed that FurE-mediated radiolabeled uracil transport was practically abolished in the respective mutants (**Figure 2B).** Only in the case of R264A mutant the apparent loss-of-function proved to be the result of abolishment of translocation to the PM, due to misfolding and ER-retention of this mutant form of FurE. This suggests that R264 participates in interactions that stabilize the expression level of FurE, in addition to its functional interaction with D28. Notice, however, that D28A substitution does not lead to FurE misfolding.[29]

In conclusion, mutations of residues proposed, via homology models and initial MDs, to be elements of specific dynamic interactions along the substrate trajectory turned out to affect FurE transport function. In particular, all residues proposed to be involved in salt bridges associated with uracil/H^+ binding and symport, namely E51-K199 and R123-D261, all led to dramatic reduction of FurE transport activity. Mutations in residues proposed to be involved in dynamic polar interactions in the outer gate (Q59A-F385-S386A) led to reduction in transport capacity, but also substrate specificity modifications. In particular, Q59A and S386A led to significant loss of uric acid, uracil or 5-FU transport, but retained apparent transport activity for allantoin, as evidence in growth tests. We also note that the F385A mutation scored as a loss-of-function mutation for all substrates, might be explained by its closeness to W130, also

important in substrate specificity. Notably, mutations T63A and S64A, which affect residues that might interact with S386 in the outer gate, also showed specific reduction of uric acid transport, but retained a significant capacity for allantoin or 5-FU accumulation, while mutations R193A and F196A led to specific reduction in uric acid transport.

Molecular Dynamics calculations

The binding mode of hydronium

Contrastingly to Mhp1, which is a Na^+-driven NCS1 symporter, all other characterized NCS1 transporters seem to function via proton symport. Nevertheless, proton interactions are not elucidated for none of them. In the case of the FurE purine/proton symporter, no experimental information is available regarding the binding site/mode of the cation. In Mhp1, the symported ion stabilizes the OO conformation for substrate binding and accumulation,[19] while in LeuT induces a conformational change.[34] To shed light on this important aspect of substrate/ion co-transport and in order to determine the proton interactions, we decided to investigate the binding of a hydronium molecule (H_3O^+) to FurE by employing Funnel-Metadynamics (FM), a cutting-edge molecular binding free-energy method developed by our group which is widely used to study ligand-protein systems.[33] FM is able to reproduce the binding process of hydronium from its fully solvated state in the extracellular environment to the binding site in the OO state, using an adaptively time-dependent bias potential deposited as a sum of Gaussian functions. Such potential accelerates the sampling along a well-defined degree of freedom called collective variable (CV), which in this case is the distance from H_3O^+ to FurE. During the FM calculations the whole binding pathway was simulated, and all the possible binding sites energetically evaluated (**Figure S4A**). The preferential binding site of hydronium was identified as the lowest energy state in the Binding Free Energy Surface (BFES) (**Figure 3A**) and proved to be the same site identified for Na^+ in Mhp1. This site is at the interface of TMSs 1 and 8, interacting with E51 (TMS1b) and T336 (TMS8) (**Figure 3B)**. The structural stability of the obtained binding complex FurE/H_3O^+ was further assessed by a 150 ns long plain MD simulation. It is worth noting that the hydronium binding mode between E51 carboxylate and T336 hydroxyl group is very similar to that in both Mhp1 and LeuT sodium co-crystallized structures, and in addition the threonine residue is conserved in all the three transporters. Finally, the residue K199 displayed increased flexibility in the presence of H_3O^+.

The binding mode of uracil

Using FM, we also simulated the binding process of uracil (K_m = 1 mM) to its putative binding site in FurE. This site was confined to TMS1, TMS3, TMS6 and TMS8 as suggested by mutagenesis data, the binding site in Mhp1 and other NCS1 transporters.[26] As performed in the case of H_3O^+, we simulated the binding process of uracil from its fully solvated state to the binding site in the Occ state, using the uracil distance to the binding site as CV. As starting structure, the uracil binding mode generated by docking was used. We note that this choice does not affect the final result, since during FM all the possible binding poses at the binding site are explored by the ligand. Knowing that hydronium is bound to the transporter in the Occ state,[19,22] we included H_3O^+ in this system occupying the binding mode previously identified by the FM calculation. In order to ensure the sampling of a wide area around the binding site we set a large cone section in the FM simulation (**Figure S4B**). Derived from the global minimum of the BFES (**Figure 3C**), the selected model of uracil binding mode (**Figure 3D**) is remarkably similar with that of (5S)-5-benzylimidazolidine-2,4-dione (hydantoin analogue) in Mhp1 crystal structure (**Figure S5**).[22] In more detail, we observed H-bonds interactions between T254 (TMS6) and uracil C2=O, N341 (TMS8) and uracil C4=O and N3, and π-π stacking interactions between W130 (TMS3) and uracil. Two additional minima were found at

higher energy values that represent intermediate binding poses of the ligand along its path to the final binding mode. At these poses, uracil appears first to interact with Q59 (TMS1b), via a bidentate interaction with N3 and C2=O, and a π-π stacking with W307 (L7 loop) (**Figure 3C**). Subsequently, it moves lower in FurE binding cavity, where it interacts with Q137 (TMS3) via a bidentate bond involving C4=O and N3 (**Figure 3D**). Noticeably, W130 of the binding pocket remained parallel to the axis of the membrane, maintaining the binding site open for the substrate. Finally, uracil and W130 are both interacting with F385 (TMS10), through π-π and T-shaped stacking interactions.

The conformational transition of FurE from OO to IO

To thoroughly describe the large-scale conformational transition of FurE, taking also into account the role of hydronium, uracil and the relative order with which they are transported, we employed a dimensionality reduction approach, called path collective variables (PCVs). This method is able to study complex chemical and biological processes involving a large number of degrees of freedom in one or two collective variables.[35] In this case, the aforementioned transitions can be discretized by providing a set of frames describing the required movement (more information in the Methods section). These frames include the positions of key atoms from the beginning to the end of the conformational change, allowing us to track the transition stage during the simulation and also accelerate its sampling through Metadynamics. The whole transition of FurE from OO to IO was investigated through two set of simulations, the first describing the OO-to-Occ transition and the second the Occ-to-IO one. For each of them, four systems were investigated considering all possible combinations of ligand stoichiometry:
i) FurE - H_3O^+ - uracil (*apo*);
ii) FurE + H_3O^+ - uracil;
iii) FurE - H_3O^+ + uracil;
iv) FurE + H_3O^+ + uracil.

In the simulations where hydronium and uracil are present, they occupy the binding mode previously identified. Looking at the FES obtained at the end of the PCV calculations, the FurE structures representing the global minimum were extracted and clustered. The centroid structure of the most populated cluster was selected and subjected to a 100ns standard MD simulation in order to assess its stability. These structures are described in detail in the following paragraphs. Moreover, the interactions between the most important residues during the simulated pathways were monitored and reported in **Figure 4A**, and the simulation time in **Table S1**.

OO-to-Occ path:
i) Apo state (FurE - H_3O^+ - uracil) - The FES shows one single, wide energy minimum between OO and Occ if compared with the other systems (**Figure 4B**). This clearly indicates that, when no ligand is present, FurE can adopt many conformations. Such flexibility was confirmed by standard MD simulations performed on the *apo* form of the OO state (**Figure S6**). Notably, in the energy minimum structures the initial part of TMS10 is positioned much closer to TMS1a with respect to the starting OO state. The relative orientation between "hash" and "bundle" motives remained very similar to Mhp1 The most stable interactions in the *apo* state are engaged by K199-T336, E51-T336 and R123-D261, while E51-K199 and R264-D28 interact at a minor extent (**Figure 4A**). Moreover, S386 and Q59 can form a water bridge interaction (**Figure S7**), while Q134 interacts with T336 through a water molecule (**Figure S8A**).
ii) Hydronium bound (FurE + H_3O^+ - uracil) - When H_3O^+ cation is bound to FurE, the FES is rather similar to that of the *apo* form, albeit the minimum is narrower indicating a reduced

flexibility of the transporter and in particular of TMS10 (**Figure 4B)**. This finding suggests that the presence of H_3O^+ influences the free energy landscape, leading TMS10 in a position competent to bind the substrate. More specifically, H_3O^+ engages a salt bridge with E51 and H-bond with T336, disrupting the bond between K199 and E51, between E51 and T336 and the water bridge between Q134 and T336. Consequently, T336 interacts only with K199 and the H-bond between T336 and Q134 is lost, making Q134 available to interact with uracil (**Figure S8B**). In line with the above-mentioned experiments, we obtained strong evidence for a tight coupling between H_3O^+ presence and substrate binding and transport.
iii) Uracil bound (FurE - H_3O^+ + uracil) – In the system where only uracil is bound to FurE, the FES minimum was located close to the Occ state (**Figure 4B**). However, in this pose the first part of TMS10 is still relatively distant to TMS1a; this event indeed characterizes the reaching of the proper Occ state as observed in the Mhp1 experimental structure (PDB ID 4D1B). Unbiased MD simulations performed on this system show that uracil is not stable in the binding pocket, leaving the binding mode after 20ns, while TMS10 fluctuated between an OO and Occ state (**Figure S6**).
iv) Hydronium and uracil bound (FurE + H_3O^+ + uracil) - In the case both hydronium and uracil are bound, the lowest energy minimum represents the Occ state (**Figure 4B)**. Comparing this FurE state to the crystallized Occ state of Mhp1, minor differences are found in TMS5, where a tilt was observed towards the IO conformation, and in TMS3 and TMS9. In particular, the interaction between F385 and W130 contributes to stabilize TMS10 in the occluded position, with a consequent motion of TMS9 that is however not observed in the Mhp1 crystal structure. Furthermore, the slight tilt of TMS5 suggests that FurE in Occ has already moved in a conformation closer to the IO state, foreshadowing a low energy barrier between the occluded and an Inward Occlude state. Additionally, binding of uracil stabilizes Q134 through an H-bond, in a position capable of making an H-bond network with Q59 and water molecules. S386 (TMS10) can interact with Q59 either via a water molecule or directly (**Figure S7**).

Taken together, our results provide unprecedented structural insight into the OO-to-Occ transition of FurE. In detail, it is clearly shown that the presence of hydronium stabilizes the FurE conformation competent for binding the uracil and that the binding of both hydronium and uracil is necessary to lock FurE in Occ state. Occ state is a very stable state as demonstrated by the low RMSD values (~1 Å) computed for the backbone Cα atoms of the transporter in unbiased MD calculations. Additionally, the break of initial bonds that stabilized TMS5 in a closed position and retained a stable hash-bundle domain orientation (K199-E51, K199-T336, E51-T336), allow the FurE structure to move towards IO state.

Occ-to-IO path
i) Hydronium and uracil bound (FurE + H_3O^+ + uracil) - When uracil and H_3O^+ are both bound to FurE, the transporter assumes a low energy structure that approaches the IO state, albeit not reaching it. This can be defined as the Inward Occluded (IOcc) state. Here, TMS3 is tilted, inducing both TMS4 and TMS5 to assume a semi-open state. At the same time the central part of TMS8 is tilted away from TMS1a. The TMS3 motion is characterized by the break of the electrostatic interaction between D261 (TMS6) and R123 (TMS3) (**Figure 4A**), which instead interacts with T254 of the uracil binding site and uracil itself. H_3O^+ in a more interior position, approaches D28 in the N-terminal loop. In addition, the E51 side chain rotates following the cation motion and this results in a more stable interaction with K252 (**Figure 4A**).
ii) Uracil bound (FurE - H_3O^+ + uracil) – In this state, the FES shows a minimum close to the IO conformation. Such minimum is narrow, confined by a high-energy barrier (**Figure 4C**). This finding suggests that first H_3O^+ unbinds FurE, then the transporter is stabilized in a close-to-IO conformation useful for uracil release. Compared to the Mhp1 inward structure, the tilt

of TMS5 is more pronounced, while TMS8 is not tilted anymore leading to a maximum distance from TMS1a. Both conformational changes elicit a rearrangement of the other helices of the "hash" motif TMS3, TMS4 and TMS9 (**Figure S9**).

iii) Apo state (FurE - H_3O^+ - uracil) - In the *apo* system, the FES shows the lowest energy minimum close to IO, in a position similar to the uracil bound state. However, here the minimum is wider, indicating a larger conformational freedom of the transporter in the *apo* state. TMS5 is rather flexible, while TMS3 is slightly bent if compared with the Occ state. As FurE assumes the *apo* state after the release of both the ligands, such conformational freedom might be instrumental to favor the reverse transition of the transporter to the outward state. The FurE flexibility was confirmed by standard MD simulations carried out on the structure of the minimum.

iv) Hydronium bound (FurE + H_3O^+ - uracil) - When only H_3O^+ is bound to FurE, the energy minimum structure is between Occ and IO (**Figure 4C**), with TMS5 very close to the position assumed in Occ. This hints that without uracil the protein is not able to reach the IO state.

Our calculations show that when H_3O^+ is still bound to the protein the conformation is stabilized in an intermediate state between Occ and IO. This suggests that the sequence of events first includes dislocation and dissociation of the H_3O^+, while the uracil is needed in order to shift to the final IO state and then is released. Furthermore, this transition from Occ to IO is related to TMS3 tilt and TMS8 shift associated also with both H_3O^+ and substrate interactions.

The internalization pathway of H_3O^+ cation

Based on our PCV calculations on the FurE Occ-to-IO transition, hydronium is the first to be released in the intracellular environment. Therefore, we investigated the unbinding of H_3O^+ from the transporter by means of FM simulations (**Figure S4C**). Our results show that hydronium is able to move towards the intracellular region of FurE passing through different binding modes (**Figure 5A, 5B**). First, H_3O^+ breaks the interactions with T336 to H-bond with S339, while maintaining the salt bridge with E5. This corresponds to minimum D in the FES reported in **Figure 5A.** Then, hydronium binds to a cleft created by F47, F262 and E51, corresponding to minimum C (**Figure 5A**). Afterwards, the interaction with E51 is lost and H_3O^+ binds to D28, D26 of the N-terminal LID[29] and N347, corresponding to minimum B of the FES (**Figure 5A**). Finally, H_3O^+ reaches the lowest energy pose A, binding to D28 and D26 (**Figure 5B**), before being fully released in the cytoplasm. The motion of E51 along with the H_3O^+ unbinding induces the break of the interactions E51-K199 and D28-R264 (**Figure 4A**). Overall, our simulations indicate that the flexibility of the N-terminal LID of FurE plays a major role in the release of hydronium in the cytoplasm.

The internalization pathway of uracil

Once hydronium unbinds, uracil can be released in the intracellular environment. We investigated the unbinding of uracil from the FurE IO state through FM calculations. In particular we investigated all the possible exiting pathways from the binding pocket to the TMS5 inner gate (**Figure S4D**). The FES and the energetically relevant poses assumed by the ligand along its exit pathway from the transporter are represented in **Figure 5C, 5D,** respectively. During uracil unbinding three residues play a major role and are W130, E51 and W39 (**Figure 5D**). W130 keeps a vertical conformation to the z axis of the membrane, thus closing *de facto* the access to the extracellular part of the transporter, while E51 forms a H-bond with uracil favoring the translocation of the ligand towards the TMS5 inner gate. Finally, W39 forms π-π and T-shaped stacking interactions with uracil justifying the relevance of W39 as highlighted by mutagenesis data. It should be noticed that W39 (TMS1) is part of a hydrophobic cleft consisting of F262 (TMS6), Y265 (TMS6), V343 (TMS8) and V189 (TMS5) contributing in the stability of the OO and Occ states where TMS1a, TMS6b, TMS8 and TMS5

are close, while in IO TMS8 and TMS5 move away as H_3O^+ and uracil are transported intracellularly. It is interesting to note that standard MD simulations carried out on the metastable states identified along the uracil unbinding led to a fast release of the ligand in the solvent, indicating that such process is barrier-less and semi-diffusive.

Discussion

The molecular basis of coupled nucleobase/proton symport is an important mechanistic aspect of NCS1 transporters. Very few cases of proton symporters have been structurally described and the structural and functional details of the transport haven't been elucidated yet, neither computationally nor experimentally. Focusing on the FurE transporter, we addressed this question by performing extended free-energy calculations, focused on substrate translocation coupled with proton symport, investigating also the large conformational rearrangement of the FurE structure that accompanies these events. In this study, proton symport was simulated by introducing H_3O^+ as a second distinct substrate. Proton binding could be probed by running MD calculations considering all different protonation combinations of Asp, Glu and His residues or by applying Quantum-mechanics/molecular-mechanics (QM/MM).[36] In the FurE case the number of possible input combinations for standard MDs grows up to 32 and is computationally very demanding and the same holds for QM/MM.

To disclose with atomic resolution the binding sites of both uracil and H_3O^+cation in FurE, we employed a state-of-the-art binding free-energy technique, named funnel-metadynamics. At variance with other binding simulative techniques, FM allows the sampling of the binding process without knowing *a priori* the binding mode of the ligand and provides a thorough classification of all possible binding modes. Independently from the initial position, the full binding mechanism will be sampled, obtaining an accurate estimate of the absolute ligand-protein binding free energy and a thorough classification of all possible binding modes. All molecular players are explicitly simulated, including water molecules, thus granting information about their dynamics during the binding process. The newly developed code of FM also incorporates a roto-translational matrix to correctly consider the entropy of the system. FM has an affordable computational cost for studying rare events such as binding processes, if compared to standard MD calculations. Lastly, it is self-diagnostic, meaning that the free energy calculation converges only to the exact value and critical points, such as non-optimal CVs or bad choice of simulation parameters, can be identified by not convergence calculations.

Our results show that H_3O^+ interacts with three negatively charged residues, namely E51, D28 and D26. The initial binding location (i.e., alongside E51) was found to be exactly at the same place where Na^+ is co-crystallized in Mhp1. According to the FES of the OO-to-Occ pathway, H_3O^+ binding stabilized the rather flexible apo structure in an intermediate conformation between the initially constructed models of OO and Occ, contributing to the conformational change from OO to Occ. The FurE-H_3O^+ interaction was found to produce rearrangements in specific residues, like inducing the availability of Q134, preparing the binding site for uracil, without however major protein conformational change. This agrees with previously reported data for Mhp1. Indeed, fluorescence quenching experiments in Mhp1[21] show that the presence of sodium increases by about tenfold the affinity for benzyl-hydantoin. Moreover, in Mhp1 it has been shown by using distance measurements between pairs of spin labels that Na^+ binding does not shift Mhp1 conformational equilibrium.[39] This dynamic behavior differs in other 5+5 folded transporters like LeuT, dDAT, hDAT, SERT, where Na^+ binding favors an occluded conformation. FRET experiments in LeuT[37] suggest a model where a cation-dependent conformational change can create and stabilize the substrate binding site. In the FurE case, only when both substrates are bound, the lowest energy conformation shifts towards the occluded structure, in which case both TMS10 (outer gate) and TMS5 (inner gate) are closed. Moreover, a relatively small change in the "hash" helices occurred. More

specifically, the relative motion of W130 probably induces a small bend in the last part of TMS3 assisted by a glycine in residue position 132 and is followed by a similar bend of the first part of TMS8. Furthermore, TMS9 follows the movement of TMS10 and induces a small shift to TMS4 (**Figure 4**). Key ligand/FurE interactions for the OO-to-Occ transition, such as uracil-W130-F385 and W130-F388, as well as minor contributions like the Q59-S386 interaction, were identified. This is in accordance with Mhp1, where a similar network of interactions is observed and explains how ligand binding stabilizes the TMS10 tilt towards the occluded conformation.[38] Importantly, mutagenesis data presented herein supported the functional importance of residues E51, W130, Q134, K199, K252, T336 and F385, derived from our *in silico* results. In the FurE transporter, substrate release to the extracellular environment in Occ is mainly impeded by W130 (TMS3). The polar residues S386 (TMS10) and Q59 (TMS1b) can also contribute to the prevention of substrate release to the extracellular solute, interacting mainly through the formation of H-bonds via intermediate water molecules. In agreement with our results, in the LeuT transporter, the substrate release from the occluded state to the extracellular is prevented by Y108 (corresponding to W130 in FurE) and F253 (TMS6), while the structure is stabilized by the interaction of D404 (TMS10) and R30 (corresponding to Q59 in FurE) through two water molecules.[10]

After both the substrate and the hydronium are bound in FurE, a conformational change leading to substrate translocation occurs. In particular, the computed FESs suggest that FurE assumes an intermediate structure between Occ and IO where H_3O^+ cation should be able to move towards the intracellular domain, as D28 loses the interaction with R264 to engage the moving hydronium. At the same time, E51 loses the interaction with K199 and interacts more with K252, unleashing the TMS5 intracellular gate, while the substrate in the binding site is destabilized as the interaction between R123 and D261 breaks and the substrate forms interactions with both R123 and T254. These events induce a relative motion of TMS3, and consequently of TMS4 and the first part of TMS5, followed by a major tilt of TMS8. In this state, we observe an initial bending of the first part of the unleashed TMS5 in P204 position opening an inner gate. This conformation can be considered as the inward-occluded state in which still both uracil and H_3O^+ cation are bound. In both LeuT[40] and DAT[41], the inward-closed (occluded) state is stabilized by a Na^+ ion bound to the Na2 site (Na2 ion), based on experimental studies. However, in LeuT-type transporters two sites have been located for sodium binding, playing key roles not only in stabilizing transporter conformations, but also in substrate binding. In fact, in LeuT, the leucine carboxyl group binds directly to Na1 and has been suggested that sodium and substrate internalization are coupled.[10] In the FurE structure, two positively charged residues are in positions close to Na1 and Na2 sites. Specifically, the K199 side chain group is in the same position of Na ion in Mhp1, which is the Na2 site, while K252 side chain shows a relative flexibility and very often is located close to the LeuT Na1 site, which does not exist in Mhp1.

In order for FurE to reach the IO state, H_3O^+ must be released, as it is evident that only in such a case the FES is shifted to IO. As a result, H_3O^+ leaves first and this event triggers the transporter transition to IO and uracil is finally released, as similarly proposed also for DAT and LeuT.[40,42–44] According to computational studies on DAT,[45] the inward open conformation is obtained after the spontaneous release of the Na^+ ion from the Na2 site. The unbinding of Na^+ happens after 800ns of unbiased MD simulations and is observed in 12 out of 50 runs of 1μs.[42] The process is mostly determined by the number of waters that penetrate the functional sites of the transporter from the intracellular region. After leaving the Na2 site, Na^+ is located between TMS5 (T269), N-terminal and TMS8 (D421 and D436). This procedure destabilizes the inward occluded state, as suggested by computational and experimental studies.[46] Internalization of hydronium implies neutralization of D28 and D26 and subsequent relocation of the N-terminal LID in agreement with our previously reported results.[29]

When only uracil is left inside the system, FurE is in the IO conformation and the substrate is ready to leave the transporter. TMS5 (the inner gate) is open, the upper part of TMS3 bends, TMS8 is not tilted anymore, while TMS4 and 9 are relocated following the relative motions of TMS5, TM8 and TMS3. H_3O^+ release, interrupted the E51-H_3O^+-T336 interaction bridging the "hash" and "bundle" motives, allowing the middle part of TMS8 to shift away from TMS1. These events alter the binding site residue positions, interactions of uracil in the binding site are not favored anymore, E51-K199 interaction is also lost resulting in TMS5 maximum bending and subsequently uracil is able to leave the binding site. Our results suggest that proton release triggers concerted conformational bending in TMS3, 5 and 8 that are possible due to the presence of G132, P204 and G335. Importantly, these findings suggest a deviation from the rigid-body motion of the "hash" motif in agreement with previous experimental evidence for Mhp1 resulted by spin label experiments.[39]

When FurE is in the *apo* form, the energy minimum structure is close to IO (**Figure** 4). This finding agrees with the evidence that Mhp1 has been crystalized also in the *apo* form conformation.[20] However, the FES minimum in the *apo* form is wide, suggesting that the transporter might assume several alternative conformations between Occ and IO. The fact that the presence of hydronium stabilizes a FurE state close to Occ as displayed in the FES (**Figure 4C**) (e.g., TMS8 tends to assume the orientation of Occ) prompts to suggest that H_3O^+ binding could be essential even for FurE's backward transition to OO. In such a case, FurE might work as antiporter, as also proposed for other transporters like SERT , DAT and LeuT.[47–49] The broad FES curves in both OO-to-Occ and Occ-to-IO transitions and the flexibility observed in TMS10 and TMS5 provides the possibility that the new symporting cycle occurs by binding of the substrate in low probability conformations shifting the equilibrium again to the Occ and finally to OO states, however, our calculations are not conclusive in this sense and further investigations are necessary.

Conclusion

In this study, we investigated using Metadynamics and mutational analysis the operation mode of the FurE proton symporter and revealed molecular details of the conformational changes necessary for uracil/H^+ symport. A schematic representation of the mechanism in represented in **Figure 6.** By systematically evaluating the differences in energy landscape of the transporter conformational transition under different combinations of proton and substrate binding, we constructed a model relating anionic and cationic residues with specific proton binding and internalization and showed how proton translocation is prerequisite for uracil transport. Furthermore, theoretical simulations identified residues critical for specific steps of uracil/H^+ transport, and mutational analysis validated these findings. Overall, we show that H_3O^+/uracil binding and transport shape the energy landscape by eliciting induced-fit conformational changes that lead to sequential movements of specific TMS in the bundle and hash domains, associated also with opening and closing of outer (TMS10) and inner (TMS5) gates. Our results infer that the hash motif helices exhibit flexibility and tilt upon substrate binding in the OO-to-Occ conformational rearrangement, while in the Occ-to-IO TMS3, 5 and 8 exhibit local substrate binding-dependent flexibility, questioning the rigid rocking-movement of the bundle or hash motifs, proposed in LeutT or Mhp1, respectively. Additionally, we show that a key step for uracil transport to be completed is the intracellular release of H_3O^+, assisted by the flexibility of N-terminal LID sequence. This view complements with critical details our understanding of the nucleobase/H+ coupling mechanism.

Materials and methods

Protein Model Construction

Model of FurE was constructed based on homology modeling using Prime 2018-4 (Schrödinger, LLC, New York, NY, 2018) on Maestro platform (Maestro, version 2018-4, Schrödinger, LLC, New York, NY, 2018). Mhp1 was used as query in the three conformations: OO(2JLN), Occ(4D1B), IO(2X79), sharing with FurE a 35% similarity, while the sequence alignment was formulated according to previous work.[29] In order to correctly represent TMS9 in the case of IO as in 2X79 IO Mhp1 crystal structure a part of it was coil, we started with the OO FurE structure and using Targeted Molecular Dynamics in plumed-v2 software,[50] a constant force of 500000 kj/(mol*nm^2) was applied on the Ca atoms of the helices to create FurE in occluded and inward state. The constant force was gradually turned to zero and the system was further subjected to stabilization.

System Setup

In order to construct the protein-ligand complex CHARMM-GUI[51] platform was used. Each model was inserted into a heterogeneous fully hydrated bilayer 120 Å × 120 Å × 120 Å, consisting of YOPC, POPI lipids and ergosterol at a ratio of 40:40:20. The membrane embedded system was solvated with TIP3P water molecules. The solution contained neutralizing counter ions and 150 mM Na^+ and 150 mM Cl^-. In the case that $H3O^+$ was present, a water molecule was replaced, and the system was neutralized with Cl^- counter ions. The assembled simulation system consisted of ~160,000 atoms.

Molecular Dynamics (MD) / Metadynamics

All simulations were conducted using GROMACS software, version 2019.2.[52] CHARMM36m[53] force field was chosen for protein and lipids, H_3O^+ was provided form Bryce group[54] while the ligand and H_3O^+ were prepared using Antechamber[55] and the general Amber force field.[56] The protein orientation into the membrane was calculated using the OPM database of the PPM server.[57] All model systems were minimized and equilibrated to obtain stable structures. Minimization was carried out for 5,000 steps with a step size of 0.001 kJ/mol applying a steepest descent followed by a conjugate gradient algorithm, and the system was equilibrated for 20ns by gradually heating and releasing the restraints to expedite stabilization. Finally, the system proceeded to further simulations free of restraints at a constant temperature of 300K using Nose-Hoover thermostat,[58] the pressure was kept constant at 1 bar using Parrinello-Rahman semi-isotropic pressure coupling[59] and compressibility at 4.5e-5 bar^{-1}. The van der Waals and electrostatic interactions were smoothly switched off at 1.2 nm, while long-range electrostatic interactions were calculated using the particle mesh Ewald method.[60] All bonds were constrained using the LINCS algorithm,[61] allowing a time-step of 2.0 fs. The trajectories were further examined for structural stability by RMSD calculation of protein Ca (up to 1.2 Å) and by visual inspection with VMD platform[62] thus ensuring that the thermalization did not cause any structural distortion.
For metadynamics[32,33,35,63] simulations the plumed-v2 software was used.[50]

Funnel-Metadynamics for H_3O^+ cation.

a) The FurE transporter used was in outward-open (OO) conformation. Since no data are available concerning the binding site of the H_3O^+ cation, a wide area around the equivalent one of the Na^+ cation in Mhp1 was circumvented by the funnel cone. The cone's starting point was T332 Ca, while the cylinder had a direction towards the extracellular waters. The funnel had a switching point between the cone and cylinder region at 4.0 nm, the amplitude of the cone was 0.27 rad, the radius of the cylinder section for the unbound region at 0.1 nm, the minimum and maximum value sampled as projection of the ligand's center of mass (COM) along the funnel axis was at 0.25 and 4.6 nm respectively, as long as, the lowest and highest value for fps.lp used to construct the funnel-shape restraint potential was at 0.00 and 4.8 nm respectively. The

value for the spring constant of the funnel-shape restraint potential was set to 5000 kj/(mol*nm^2). As collective variable (CV) was selected the distance between the Ca atom of T332 and the center of mass of H_3O^+ cation. The width of the Gaussian functions was set to 0.05 nm, the height to 2 kj/mol and the deposition stride to 500 simulation steps. The rescaling factor of the Gaussian function's height was 20 as we performed well-tempered metadynamics.

b) The study of binding/unbinding process of the H_3O^+ cation in the cytoplasmic solvent was initiated by using well-tempered metadynamics with the FM method on FurE in the Occ state of FurE. Uracil was included in the system, placed at the binding site, whereas an upper wall of 20000 kj/(mol*nm^2) enforced the COM in distances lower than 0.9 nm from the Cg of N341. The constructed funnel included all the possible routes that could lead the H_3O^+ to the exit to the cytoplasm. The cone region started at Ca of S56. The direction of the funnel axis was cytoplasm-oriented passing through Asp348 Cb atom. The switching point between the cone and the cylinder region was at 3.6 nm, the amplitude of the cone section was set to 0.5 rad and the radius of the cylinder for the unbound region to 0.1 nm. The minimum and maximum value sampled as projection of the ligand's COM along the funnel axis was set to 0.29 and 4.2 nm respectively, the lowest and highest value for fps.lp used to construct the funnel-shape restraint potential was set to 0.2 and 4.3 nm respectively, while, the value for the spring constant of the funnel-shape restraint potential to 7000 kj/(mol*nm^2). As CV was selected the distance between the Ca of E51 and the center of mass of H_3O^+ cation. The width of the Gaussian functions was calculated at 0.01 nm, the height was arranged at 2 kj/mol with a rescaling factor of the Gaussian function at 20 and the deposition stride was set to 500 simulation steps.

Funnel-Metadynamics for Uracil

a) FM were performed aiming to highlight the binding mode of uracil in the binding site and the binding mechanism as it approaches the binding pocket from the extracellular. FurE was in the occluded state and the H_3O^+ cation was included in the system, as in crystallographic results of other transporters, in particular Mhp1, ion and substrate co-exist in the Occ state . In detail, the funnel used, oriented from Ca atom of V323 deep in the binding area, with direction of the funnel axis to the extracellular solute. The switching point between the cone and cylinder region was set to 2.7 nm, the amplitude of the cone section to 0.37 rad, the radius of the cylinder section for the unbound region to 0.1 nm, the minimum and maximum value sampled as projection of the ligand's COM along the funnel axis to 0.2 and 3.3 nm respectively, the lowest and highest value for fps.lp used to construct the funnel-shape restraint potential to 0.05 and 3.6 nm respectively. The value for the spring constant of the funnel-shape restraint potential was 30000 kj/(mol*nm^2). As CV was selected the distance between the Ca of N341 and the center of mass of uracil. The width of the Gaussian functions was 0.01 nm, the height was arranged at 2 kj/mol and the deposition stride at 500 simulation steps. The rescaling factor of the Gaussian function's height was 20.

b) The uracil internalization process was implemented using again, well-tempered metadynamics with the FM method, on FurE transporter in IO conformation containing uracil and not H_3O^+, as the latter was already proved from PCV simulations that leaves first the transporter in order to allow uracil to exit too (see Main Text). The funnel was constructed as to include all the possible exiting pathways from the binding pocket to the TMS5 outer gate. The cone restraint started at backbone C atom of PF53, while the direction of the funnel axis was cytoplasm-oriented passing through S342 O atom. The switching point between the cone and the cylinder region was set to 3.4 nm, the amplitude of the cone section to 0.49 rad and the radius of the cylinder for the unbound region to 0.1 nm. The minimum and maximum value sampled as projection of the ligand's COM along the funnel axis was set to 0.21 and 4.1 nm respectively, the lowest and highest value for fps.lp used to construct the funnel-shape restraint potential was set to 0.1 and 4.2 nm respectively, while, the value for the spring constant of the

funnel-shape restraint potential was set to 30000 kj/(mol*nm^2). As CV was chosen the distance between the backbone of A50 and the center of mass of uracil. The width of the Gaussian functions was calculated at 0.01 nm, the height was arranged at 2 kj/mol with a rescaling factor of the Gaussian function at 20 and the deposition stride was set to 500 simulation steps.

Metadynamics Simulations with Path Collective Variable (PCV):

a) OO-to-Occ path: In this case we used the Cα atoms of the residues belonging to FurE helices involved in hash and bundle motif. This choice was found to be appropriate because the calculated FESs were well reproducible. The initial path was obtained through a carefully chosen set of frames with equally distant RMSDs, derived from a steered MD simulation where the OO FurE was biased to Occ conformation using a stable force on Ca atoms of helices. 6 frames were used to construct the path in total, while the average distance between adjacent frames was 0.13 nm. The RMSD matrix was constructed and plotted, confirming that the frames where appropriate for the calculation. The λ value calculated for s was equal to 200 nm^2. The width of the Gaussian functions for hills deposition was 0.035 nm^2 based on the structure fluctuation in unbiased MD, the height was arranged at 0.5 kj/mol and the deposition stride at 500 simulation steps. An upper wall of 500000 kj/(mol*nm^2) was set to constrain the distance from the path at a value lower than 0.06, based in unbiased MD simulations of more than 200 ns where the cv's fluctuation did not reach values higher than 0.03. If uracil is part of the system, it is constrained in the previously calculated position in the binding site with a distance restraint of 20000 kj/(mol*nm^2) at 0.7 nm between the center of mass of the substrate and Cd atom of Q134. The same constraint was applied on the distance of H_3O^+ cation from Cd atom of E51 at 0.45 nm.

b) The same rationale and method were used in the Occ-to-IO case. Here, the λ value for s was equal to 110 nm^{-2}, the width of the Gaussian functions for hills deposition was 0.037 nm^2, the upper wall of 500000 kj/(mol*nm^2) was set to constrain the z at a value lower than 0.1.

Media, strains and growth conditions

Standard complete (CM) and minimal media (MM) for *A. nidulans* growth were used, supplemented with necessary auxotrophies at concentrations given in http://www.fgsc.net. Glucose 1% (w/v) was used as carbon source. 10 mM of sodium nitrate (NO_3^-) or 0.5 mM of uric acid (UA), xanthine (XAN) or allantoin (ALL) were used as nitrogen sources. The uracil toxic analog 5-FU was used at 100 μM in the presence of 10 mM NO_3^- as N source. All media and chemical reagents were obtained from Sigma-Aldrich (Life Science Chemilab SA, Hellas) or AppliChem (Bioline Scientific SA, Hellas).

A *ΔfurD::riboBΔfurA::riboBΔfcyB::argBΔazgAΔuapAΔuapC::AfpyrGΔcntA::riboB pabaA1 pantoB100* mutant strain named Δ7, was the recipient strain in transformations with plasmids carrying FurE mutant versions, based on complementation of the pantothenic acid auxotrophy *pantoB100.*[64] The Δ7 strain has an intact endogenous FurE gene transporter, but this is very little expressed under standard conditions and thus does not contribute to detectable transport of its physiological substrates (UA, ALL) or to sensitivity in 5-FU[26]*A. nidulans protoplast isolation and transformation was performed as previously described*.[65] Growth tests were performed at 37 °C for 48 h, at pH 6.8.

Standard molecular biology manipulations and plasmid construction

Genomic DNA extraction from *A. nidulans* was performed as described in FGSC (http://www.fgsc.net). Plasmids, prepared in *Escherichia coli*, and DNA restriction or PCR fragments were purified from agarose 1% gels with the Nucleospin Plasmid Kit or Nucleospin Extract II kit, according to the manufacturer's instructions (Macherey–Nagel, Lab Supplies Scientific SA, Hellas). Standard PCR reactions were performed using KAPATaq DNA

polymerase (Kapa Biosystems). PCR products used for cloning, sequencing and re-introduction by transformation in *A. nidulans* were amplified by a high-fidelity KAPA HiFi HotStart Ready Mix (Kapa Biosystems) polymerase. DNA sequences were determined by VBC-Genomics (Vienna, Austria). Site-directed mutagenesis was carried out according to the instructions accompanying the Quik-Change® Site-Directed Mutagenesis Kit (Agilent Technologies, Stratagene). The principal vector used for most *A. nidulans* mutants is a modified pGEM-T-easy vector carrying a version of the *gpdA* promoter, the *trpC* 3′ termination region and the *panB* selection marker.[26] Mutations in FurE were constructed by oligonucleotide-directed mutagenesis or appropriate forward and reverse primers. Transformants with intact FurE alleles were identified by PCR analysis.

Epifluorescence microscopy

Samples for standard epifluorescence microscopy were prepared as previously described.[66]
In brief, sterile 35-mm l-dishes with a glass bottom (Ibidi, Germany) containing liquid MM supplemented with $NaNO_3$ and 0.1% glucose were inoculated from a spore solution and incubated for 18 h at 25 °C. The samples were observed on an Axioplan Zeiss phase contrast epifluorescent microscope, and the resulting images were acquired with a Zeiss-MRC5 digital camera using the AxioVs40 V4.40.0 software. Images were processed using the Adobe Photoshop CS3 software for brightness adjustment, rotation and alignment.

Uptake assays

FurE transport activity was measured by estimating uptake rates of [^{3}H]-uracil (40 Ci mmol^{-1}, Moravek Biochemicals, CA, USA), as previously described.[64]
In brief, [^{3}H]-uracil uptake was assayed in *A. nidulans* conidiospores germinating for 4 h at 37 °C, at 140 rpm, in liquid MM (pH 6.8). Initial velocities were measured on 10^7 conidiospores/100 μL incubated with A concentration of 0.2μM of [^{3}H]-uracil at 37 °C. All transport assays were carried out in triplicates in at least two independent experiments. Results were analyzed using the GraphPad Prism software.

Acknowledgments

This research was funded by a Stavros Niarchos Foundation research grant. I.Z was supported by a Stavros S. Niarchos Foundations scholarship in National and Kapodistrian University of Athens and by a COST action scholarship in Università della Svizzera Italiana. Work in the laboratory of George Diallinas is supported by Foundation Santé. This work was also supported by computational time granted from the Greek Research & Technology Network (GRNET) in the National HPC Facility "ARIS" under project pr010020. We would like to thank Dr. Simone Aureli for his assistance on the computational part, Dr. Paolo Conflitti and Dr. George Lambrinidis for many helpful discussions.

Author contributions: The project was initiated by GD and EM. IZ carried out the calculations with help by SR and supervision by EM and VL. GFP and YP carried out the experiments supervised by GD. The manuscript was prepared by IZ, EM and GD and all authors contributed by thoroughly revising it.

Competing interests: Authors declare no competing interests.

References

(1) Jardetzky, O. Simple Allosteric Model for Membrane Pumps. *Nature* **1966**, *211* (5052), 969–970. https://doi.org/10.1038/211969a0.

(2) Drew, D.; Boudker, O. Shared Molecular Mechanisms of Membrane Transporters. *Annu. Rev. Biochem.* **2016**, *85* (1), 543–572. https://doi.org/10.1146/annurev-biochem-060815-014520.

(3) Penmatsa, A.; Gouaux, E. How LeuT Shapes Our Understanding of the Mechanisms of Sodium-Coupled Neurotransmitter Transporters. *J. Physiol.* **2014**, *592* (5), 863–869. https://doi.org/10.1113/jphysiol.2013.259051.

(4) Forrest, L. R.; Zhang, Y.-W.; Jacobs, M. T.; Gesmonde, J.; Xie, L.; Honig, B. H.; Rudnick, G. Mechanism for Alternating Access in Neurotransmitter Transporters. *Proc. Natl. Acad. Sci. U. S. A.* **2008**, *105* (30), 10338–10343. https://doi.org/10.1073/pnas.0804659105.

(5) Kazmier, K.; Claxton, D. P.; Mchaourab, H. S. Alternating Access Mechanisms of LeuT-Fold Transporters: Trailblazing towards the Promised Energy Landscapes. *Curr. Opin. Struct. Biol.* **2017**, *45*, 100–108. https://doi.org/10.1016/j.sbi.2016.12.006.

(6) Krishnamurthy, H.; Piscitelli, C. L.; Gouaux, E. Unlocking the Molecular Secrets of Sodium-Coupled Transporters. *Nature* **2009**, *459* (7245), 347–355. https://doi.org/10.1038/nature08143.

(7) Forrest, L. R.; Rudnick, G. The Rocking Bundle: A Mechanism for Ion-Coupled Solute Flux by Symmetrical Transporters. *Physiol. Bethesda Md* **2009**, *24*, 377–386. https://doi.org/10.1152/physiol.00030.2009.

(8) Yan, N. Structural Biology of the Major Facilitator Superfamily Transporters. *Annu. Rev. Biophys.* **2015**, *44* (1), 257–283. https://doi.org/10.1146/annurev-biophys-060414-033901.

(9) Garaeva, A. A.; Slotboom, D. J. Elevator-Type Mechanisms of Membrane Transport. *Biochem. Soc. Trans.* **2020**, *48* (3), 1227–1241. https://doi.org/10.1042/BST20200290.

(10) Yamashita, A.; Singh, S. K.; Kawate, T.; Jin, Y.; Gouaux, E. Crystal Structure of a Bacterial Homologue of Na+/Cl--Dependent Neurotransmitter Transporters. *Nature* **2005**, *437* (7056), 215–223. https://doi.org/10.1038/nature03978.

(11) Wang, K. H.; Penmatsa, A.; Gouaux, E. Neurotransmitter and Psychostimulant Recognition by the Dopamine Transporter. *Nature* **2015**, *521* (7552), 322–327. https://doi.org/10.1038/nature14431.

(12) Coleman, J. A.; Navratna, V.; Antermite, D.; Yang, D.; Bull, J. A.; Gouaux, E. Chemical and Structural Investigation of the Paroxetine-Human Serotonin Transporter Complex. *eLife* **2020**, *9*, e56427. https://doi.org/10.7554/eLife.56427.

(13) Quick, M.; Abramyan, A. M.; Wiriyasermkul, P.; Weinstein, H.; Shi, L.; Javitch, J. A. The LeuT-Fold Neurotransmitter:Sodium Symporter MhsT Has Two Substrate Sites. *Proc. Natl. Acad. Sci.* **2018**, *115* (34), E7924–E7931. https://doi.org/10.1073/pnas.1717444115.

(14) Faham, S.; Watanabe, A.; Besserer, G. M.; Cascio, D.; Specht, A.; Hirayama, B. A.; Wright, E. M.; Abramson, J. The Crystal Structure of a Sodium Galactose Transporter Reveals Mechanistic Insights into Na+/Sugar Symport. *Science* **2008**, *321* (5890), 810–814. https://doi.org/10.1126/science.1160406.

(15) Ressl, S.; Terwisscha van Scheltinga, A. C.; Vonrhein, C.; Ott, V.; Ziegler, C. Molecular Basis of Transport and Regulation in the Na(+)/Betaine Symporter BetP. *Nature* **2009**, *458* (7234), 47–52. https://doi.org/10.1038/nature07819.

(16) Tang, L.; Bai, L.; Wang, W.; Jiang, T. Crystal Structure of the Carnitine Transporter and Insights into the Antiport Mechanism. *Nat. Struct. Mol. Biol.* **2010**, *17* (4), 492–496. https://doi.org/10.1038/nsmb.1788.
(17) Fang, Y.; Jayaram, H.; Shane, T.; Kolmakova-Partensky, L.; Wu, F.; Williams, C.; Xiong, Y.; Miller, C. Structure of a Prokaryotic Virtual Proton Pump at 3.2 Å Resolution. *Nature* **2009**, *460* (7258), 1040–1043. https://doi.org/10.1038/nature08201.
(18) Shaffer, P. L.; Goehring, A.; Shankaranarayanan, A.; Gouaux, E. Structure and Mechanism of a Na+independent Amino Acid Transporter. *Science* **2009**, *325* (5943), 1010–1014. https://doi.org/10.1126/science.1176088.
(19) Weyand, S.; Cameron, A. D.; Shimamura, T.; Beckstein, O.; Sansom, M. S. P.; Iwata, S.; Henderson, P. J. F. The alternating access mechanism of transport as observed in the sodium-hydantoin transporter Mhp1 https://www.ncbi.nlm.nih.gov/pmc/articles/PMC3004247/ (accessed 2020 -03 -26).
(20) Shimamura, T.; Weyand, S.; Beckstein, O.; Rutherford, N. G.; Hadden, J. M.; Sharples, D.; Sansom, M. S. P.; Iwata, S.; Henderson, P. J. F.; Cameron, A. D. Molecular Basis of Alternating Access Membrane Transport by the Sodium-Hydantoin Transporter Mhp1. *Science* **2010**, *328* (5977), 470–473. https://doi.org/10.1126/science.1186303.
(21) Weyand, S.; Shimamura, T.; Yajima, S.; Suzuki, S.; Mirza, O.; Krusong, K.; Carpenter, E. P.; Rutherford, N. G.; Hadden, J. M.; O'Reilly, J.; Ma, P.; Saidijam, M.; Patching, S. G.; Hope, R. J.; Norbertczak, H. T.; Roach, P. C. J.; Iwata, S.; Henderson, P. J. F.; Cameron, A. D. Structure and Molecular Mechanism of a Nucleobase-Cation-Symport-1 Family Transporter. *Science* **2008**, *322* (5902), 709–713. https://doi.org/10.1126/science.1164440.
(22) Simmons, K. J.; Jackson, S. M.; Brueckner, F.; Patching, S. G.; Beckstein, O.; Ivanova, E.; Geng, T.; Weyand, S.; Drew, D.; Lanigan, J.; Sharples, D. J.; Sansom, M. S.; Iwata, S.; Fishwick, C. W.; Johnson, A. P.; Cameron, A. D.; Henderson, P. J. Molecular Mechanism of Ligand Recognition by Membrane Transport Protein, Mhp1. *EMBO J.* **2014**, *33* (16), 1831–1844. https://doi.org/10.15252/embj.201387557.
(23) Pantazopoulou, A.; Diallinas, G. Fungal Nucleobase Transporters. *FEMS Microbiol. Rev.* **2007**, *31* (6), 657–675. https://doi.org/10.1111/j.1574-6976.2007.00083.x.
(24) Hamari, Z.; Amillis, S.; Drevet, C.; Apostolaki, A.; Vágvölgyi, C.; Diallinas, G.; Scazzocchio, C. Convergent Evolution and Orphan Genes in the Fur4p-like Family and Characterization of a General Nucleoside Transporter in *Aspergillus Nidulans*. *Mol. Microbiol.* **2009**, *73* (1), 43–57. https://doi.org/10.1111/j.1365-2958.2009.06738.x.
(25) Krypotou, E.; Kosti, V.; Amillis, S.; Myrianthopoulos, V.; Mikros, E.; Diallinas, G. Modeling, Substrate Docking, and Mutational Analysis Identify Residues Essential for the Function and Specificity of a Eukaryotic Purine-Cytosine NCS1 Transporter *. *J. Biol. Chem.* **2012**, *287* (44), 36792–36803. https://doi.org/10.1074/jbc.M112.400382.
(26) Krypotou, E.; Evangelidis, T.; Bobonis, J.; Pittis, A. A.; Gabaldón, T.; Scazzocchio, C.; Mikros, E.; Diallinas, G. Origin, Diversification and Substrate Specificity in the Family of NCS1/FUR Transporters: Origin and Specificity of Fur Transporters. *Mol. Microbiol.* **2015**, *96* (5), 927–950. https://doi.org/10.1111/mmi.12982.
(27) Sioupouli, G.; Lambrinidis, G.; Mikros, E.; Amillis, S.; Diallinas, G. Cryptic Purine Transporters in Aspergillus Nidulans Reveal the Role of Specific Residues in the Evolution of Specificity in the NCS1 Family. *Mol. Microbiol.* **2017**, *103* (2), 319–332. https://doi.org/10.1111/mmi.13559.
(28) Papadaki, G. F.; Amillis, S.; Diallinas, G. Substrate Specificity of the FurE Transporter Is Determined by Cytoplasmic Terminal Domain Interactions. *Genetics* **2017**, *207* (4), 1387–1400. https://doi.org/10.1534/genetics.117.300327.

(29) Papadaki, G. F.; Lambrinidis, G.; Zamanos, A.; Mikros, E.; Diallinas, G. Cytosolic N- and C-Termini of the Aspergillus Nidulans FurE Transporter Contain Distinct Elements That Regulate by Long-Range Effects Function and Specificity. *J. Mol. Biol.* **2019**, *431* (19), 3827–3844. https://doi.org/10.1016/j.jmb.2019.07.013.
(30) Girke, C.; Daumann, M.; Niopek-Witz, S.; MÃ¶hlmann, T. Nucleobase and Nucleoside Transport and Integration into Plant Metabolism. *Front. Plant Sci.* **2014**, *5*. https://doi.org/10.3389/fpls.2014.00443.
(31) Sucic, S.; Dallinger, S.; Zdrazil, B.; Weissensteiner, R.; Jørgensen, T. N.; Holy, M.; Kudlacek, O.; Seidel, S.; Cha, J. H.; Gether, U.; Newman, A. H.; Ecker, G. F.; Freissmuth, M.; Sitte, H. H. The N Terminus of Monoamine Transporters Is a Lever Required for the Action of Amphetamines *. *J. Biol. Chem.* **2010**, *285* (14), 10924–10938. https://doi.org/10.1074/jbc.M109.083154.
(32) Laio, A.; Parrinello, M. Escaping Free-Energy Minima. *Proc. Natl. Acad. Sci.* **2002**, *99* (20), 12562–12566. https://doi.org/10.1073/pnas.202427399.
(33) Limongelli, V.; Bonomi, M.; Parrinello, M. Funnel Metadynamics as Accurate Binding Free-Energy Method. *Proc. Natl. Acad. Sci.* **2013**, *110* (16), 6358–6363. https://doi.org/10.1073/pnas.1303186110.
(34) Gedeon, P. C.; Indarte, M.; Surratt, C. K.; Madura, J. D. Molecular Dynamics of Leucine and Dopamine Transporter Proteins in a Model Cell Membrane Lipid Bilayer. *Proteins* **2010**, *78* (4), 797–811. https://doi.org/10.1002/prot.22601.
(35) Branduardi, D.; Gervasio, F. L.; Parrinello, M. From A to B in Free Energy Space. *J. Chem. Phys.* **2007**, *126* (5), 054103. https://doi.org/10.1063/1.2432340.
(36) Jiang, T.; Wen, P.-C.; Trebesch, N.; Zhao, Z.; Pant, S.; Kapoor, K.; Shekhar, M.; Tajkhorshid, E. Computational Dissection of Membrane Transport at a Microscopic Level. *Trends Biochem. Sci.* **2020**, *45* (3), 202–216. https://doi.org/10.1016/j.tibs.2019.09.001.
(37) Claxton, D. P.; Quick, M.; Shi, L.; de Carvalho, F. D.; Weinstein, H.; Javitch, J. A.; Mchaourab, H. S. Ion/Substrate-Dependent Conformational Dynamics of a Bacterial Homolog of Neurotransmitter:Sodium Symporters. *Nat. Struct. Mol. Biol.* **2010**, *17* (7), 822–829. https://doi.org/10.1038/nsmb.1854.
(38) Kazmier, K.; Sharma, S.; Quick, M.; Islam, S. M.; Roux, B.; Weinstein, H.; Javitch, J. A.; McHaourab, H. S. Conformational Dynamics of Ligand-Dependent Alternating Access in LeuT. *Nat. Struct. Mol. Biol.* **2014**, *21* (5), 472–479. https://doi.org/10.1038/nsmb.2816.
(39) Kazmier, K.; Sharma, S.; Islam, S. M.; Roux, B.; Mchaourab, H. S. Conformational Cycle and Ion-Coupling Mechanism of the Na+/Hydantoin Transporter Mhp1. *Proc. Natl. Acad. Sci.* **2014**, *111* (41), 14752–14757. https://doi.org/10.1073/pnas.1410431111.
(40) Shi, L.; Quick, M.; Zhao, Y.; Weinstein, H.; Javitch, J. A. The Mechanism of a Neurotransmitter:Sodium Symporter – Inward Release of Na+ and Substrate Is Triggered by Substrate in a Second Binding Site. *Mol. Cell* **2008**, *30* (6), 667–677. https://doi.org/10.1016/j.molcel.2008.05.008.
(41) Borre, L.; Andreassen, T. F.; Shi, L.; Weinstein, H.; Gether, U. The Second Sodium Site in the Dopamine Transporter Controls Cation Permeation and Is Regulated by Chloride. *J. Biol. Chem.* **2014**, *289* (37), 25764–25773. https://doi.org/10.1074/jbc.M114.574269.
(42) Razavi, A. M.; Khelashvili, G.; Weinstein, H. A Markov State-Based Quantitative Kinetic Model of Sodium Release from the Dopamine Transporter. *Sci. Rep.* **2017**, *7*. https://doi.org/10.1038/srep40076.
(43) Malinauskaite, L.; Quick, M.; Reinhard, L.; Lyons, J. A.; Yano, H.; Javitch, J. A.; Nissen, P. A Mechanism for Intracellular Release of Na+ by Neurotransmitter: Sodium

Symporters. *Nat. Struct. Mol. Biol.* **2014**, *21* (11), 1006–1012. https://doi.org/10.1038/nsmb.2894.
(44) Zhao, C.; Noskov, S. Y. The Role of Local Hydration and Hydrogen-Bonding Dynamics in Ion and Solute Release from Ion-Coupled Secondary Transporters. *Biochemistry* **2011**, *50* (11), 1848–1856. https://doi.org/10.1021/bi101454f.
(45) Khelashvili, G.; Stanley, N.; Sahai, M. A.; Medina, J.; LeVine, M. V.; Shi, L.; De Fabritiis, G.; Weinstein, H. Spontaneous Inward Opening of the Dopamine Transporter Is Triggered by PIP2-Regulated Dynamics of the N-Terminus. *ACS Chem. Neurosci.* **2015**, *6* (11), 1825–1837. https://doi.org/10.1021/acschemneuro.5b00179.
(46) Kniazeff, J.; Shi, L.; Loland, C. J.; Javitch, J. A.; Weinstein, H.; Gether, U. An Intracellular Interaction Network Regulates Conformational Transitions in the Dopamine Transporter. *J. Biol. Chem.* **2008**, *283* (25), 17691–17701. https://doi.org/10.1074/jbc.M800475200.
(47) Khelashvili, G.; Schmidt, S. G.; Shi, L.; Javitch, J. A.; Gether, U.; Loland, C. J.; Weinstein, H. Conformational Dynamics on the Extracellular Side of LeuT Controlled by Na+ and K+ Ions and the Protonation State of Glu290. *J. Biol. Chem.* **2016**, *291* (38), 19786–19799. https://doi.org/10.1074/jbc.M116.731455.
(48) Khelashvili, G.; Stanley, N.; Sahai, M. A.; Medina, J.; LeVine, M. V.; Shi, L.; De Fabritiis, G.; Weinstein, H. Spontaneous Inward Opening of the Dopamine Transporter Is Triggered by PIP2-Regulated Dynamics of the N-Terminus. *ACS Chem. Neurosci.* **2015**, *6* (11), 1825–1837. https://doi.org/10.1021/acschemneuro.5b00179.
(49) Torres, G.; Gainetdinov, R.; Caron, M. Torres, G.E., Gainetdinov, R.R. & Caron, M.G. Plasma Membrane Monoamine Transporters: Structure, Regulation and Function. Nat. Rev. Neurosci. 4, 13-25. *Nat. Rev. Neurosci.* **2003**, *4*, 13–25. https://doi.org/10.1038/nrn1008.
(50) Tribello, G. A.; Bonomi, M.; Branduardi, D.; Camilloni, C.; Bussi, G. PLUMED 2: New Feathers for an Old Bird. *Comput. Phys. Commun.* **2014**, *185* (2), 604–613. https://doi.org/10.1016/j.cpc.2013.09.018.
(51) CHARMM-GUI: A web-based graphical user interface for CHARMM - Jo - 2008 - Journal of Computational Chemistry - Wiley Online Library https://onlinelibrary.wiley.com/doi/full/10.1002/jcc.20945 (accessed 2021 -05 -20).
(52) Abraham, M. J.; Murtola, T.; Schulz, R.; Páll, S.; Smith, J. C.; Hess, B.; Lindahl, E. GROMACS: High Performance Molecular Simulations through Multi-Level Parallelism from Laptops to Supercomputers. *SoftwareX* **2015**, *1–2*, 19–25. https://doi.org/10.1016/j.softx.2015.06.001.
(53) Huang, J.; Rauscher, S.; Nawrocki, G.; Ran, T.; Feig, M.; de Groot, B. L.; Grubmüller, H.; MacKerell, A. D. CHARMM36m: An Improved Force Field for Folded and Intrinsically Disordered Proteins. *Nat. Methods* **2017**, *14* (1), 71–73. https://doi.org/10.1038/nmeth.4067.
(54) AMBER parameter database (Bryce Group: Computational Biophysics and Drug Design - University of Manchester) http://amber.manchester.ac.uk/ (accessed 2021 -06 -09).
(55) Wang, L.; Berne, B. J.; Friesner, R. A. On Achieving High Accuracy and Reliability in the Calculation of Relative Protein-Ligand Binding Affinities. *Proc. Natl. Acad. Sci.* **2012**, *109* (6), 1937–1942. https://doi.org/10.1073/pnas.1114017109.
(56) Wang, J.; Wolf, R. M.; Caldwell, J. W.; Kollman, P. A.; Case, D. A. Development and Testing of a General Amber Force Field. *J. Comput. Chem.* **2004**, *25* (9), 1157–1174. https://doi.org/10.1002/jcc.20035.
(57) Lomize, M. A.; Pogozheva, I. D.; Joo, H.; Mosberg, H. I.; Lomize, A. L. OPM Database and PPM Web Server: Resources for Positioning of Proteins in Membranes. *Nucleic Acids Res.* **2012**, *40* (D1), D370–D376. https://doi.org/10.1093/nar/gkr703.

(58) Evans, D. J.; Holian, B. L. The Nose–Hoover Thermostat. *J. Chem. Phys.* **1985**, *83* (8), 4069–4074. https://doi.org/10.1063/1.449071.
(59) Parrinello, M.; Rahman, A. Polymorphic Transitions in Single Crystals: A New Molecular Dynamics Method. *J. Appl. Phys.* **1981**, *52* (12), 7182–7190. https://doi.org/10.1063/1.328693.
(60) Darden, T.; York, D.; Pedersen, L. Particle Mesh Ewald: An N·log(N) Method for Ewald Sums in Large Systems. *J. Chem. Phys.* **1993**, *98* (12), 10089–10092. https://doi.org/10.1063/1.464397.
(61) Hess, B.; Bekker, H.; Berendsen, H. J. C.; Fraaije, J. G. E. M. LINCS: A Linear Constraint Solver for Molecular Simulations. *J. Comput. Chem.* **1997**, *18* (12), 1463–1472. https://doi.org/10.1002/(SICI)1096-987X(199709)18:12<1463::AID-JCC4>3.0.CO;2-H.
(62) Humphrey, W.; Dalke, A.; Schulten, K. VMD: Visual Molecular Dynamics. *J. Mol. Graph.* **1996**, *14* (1), 33–38. https://doi.org/10.1016/0263-7855(96)00018-5.
(63) Raniolo, S.; Limongelli, V. Ligand Binding Free-Energy Calculations with Funnel Metadynamics. *Nat. Protoc.* **2020**, *15* (9), 2837–2866. https://doi.org/10.1038/s41596-020-0342-4.
(64) Krypotou, E.; Diallinas, G. Transport Assays in Filamentous Fungi: Kinetic Characterization of the UapC Purine Transporter of Aspergillus Nidulans. *Fungal Genet. Biol. FG B* **2014**, *63*, 1–8. https://doi.org/10.1016/j.fgb.2013.12.004.
(65) Koukaki, M.; Giannoutsou, E.; Karagouni, A.; Diallinas, G. A Novel Improved Method for Aspergillus Nidulans Transformation. *J. Microbiol. Methods* **2003**, *55* (3), 687–695. https://doi.org/10.1016/s0167-7012(03)00208-2.
(66) Gournas, C.; Amillis, S.; Vlanti, A.; Diallinas, G. Transport-Dependent Endocytosis and Turnover of a Uric Acid-Xanthine Permease. *Mol. Microbiol.* **2010**, *75* (1), 246–260. https://doi.org/10.1111/j.1365-2958.2009.06997.x.

FIGURES

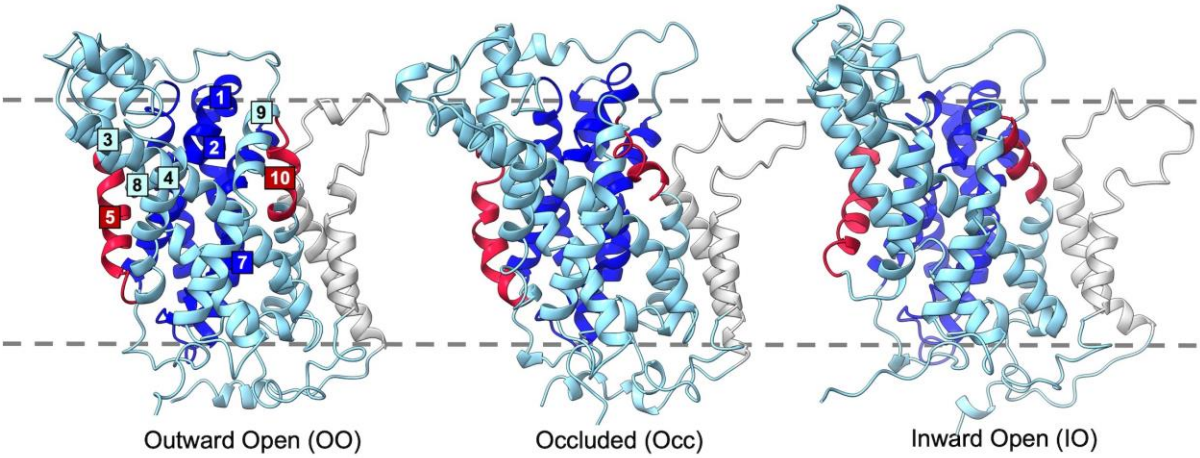

Figure 1: The three homology model structures of FurE (Outward Open, Occluded, Inward Open) based on corresponding Mhp1 template crystal structures shown in a side view (orientation parallel to the membrane lipids). The "bundle" helices are colored blue, the "hash" helices are colored cyan, the outer and inner gates are colored red and the TMS11, and TMS12 are grey. The yellow dashed lines represent the membrane plane.

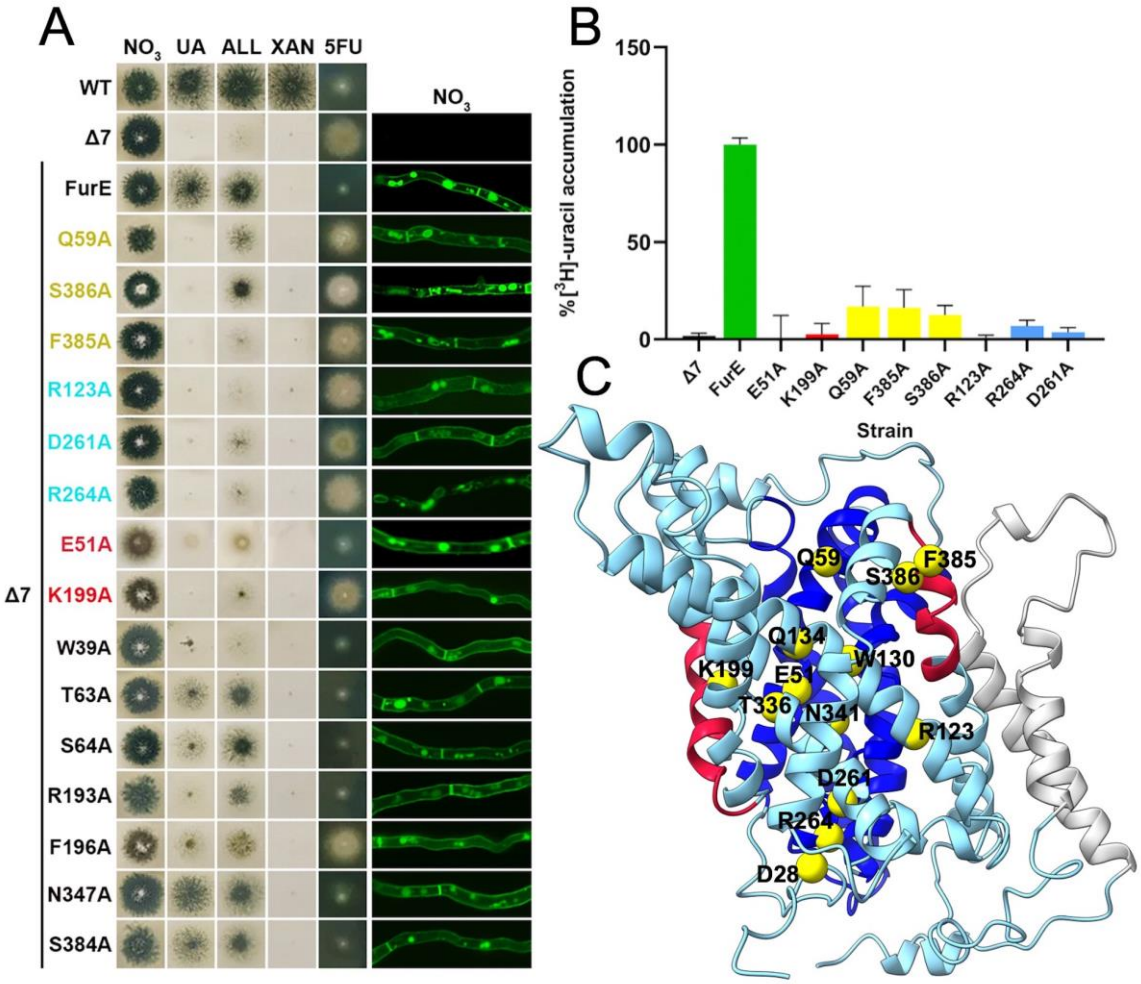

Figure 2: Functional analysis of FurE mutants. **(A)** Growth tests of isogenic strains expressing distinct FurE mutant versions in a Δ7 genetic background (i.e. genetically lacking other nucleobase-related transporters), compared to a positive (FurE) and a negative (Δ7) control strain (for strain details see materials and methods). NO_3, UA, ALL, Xan denote MM supplemented with nitrate, uric acid, allantoin or xanthine as sole N source. 5FU is MM+NO_3 supplemented with 5-FU. WT denotes a standard *A. nidulans* wild-type strain expressing all major nucleobase transporters. *In vivo* epifluorescence microscopy of the same strains is shown in the right panel. All FurE mutants are functionally tagged with GFP. Notice that all FurE mutant versions, except R264A, exhibit normal (i.e. wt FurE-like) plasma membrane localization and vacuolar turnover. R264A is trapped in the perinuclear ER rings, typical of misfolded versions of FurE or other transporters (for details see Materials and methods)
(B) Direct uptake assays of selected FurE mutants, using 0.2 μM [^{3}H]-radiolabeled uracil. The figure shows relative % initial uptake rates (1 min) of mutants, when wild-type FurE transport is taken as 100%, performed with 10^7 germinated conidiospores, as described by Krypotou and Diallinas, 2014 (for details see Materials and methods)

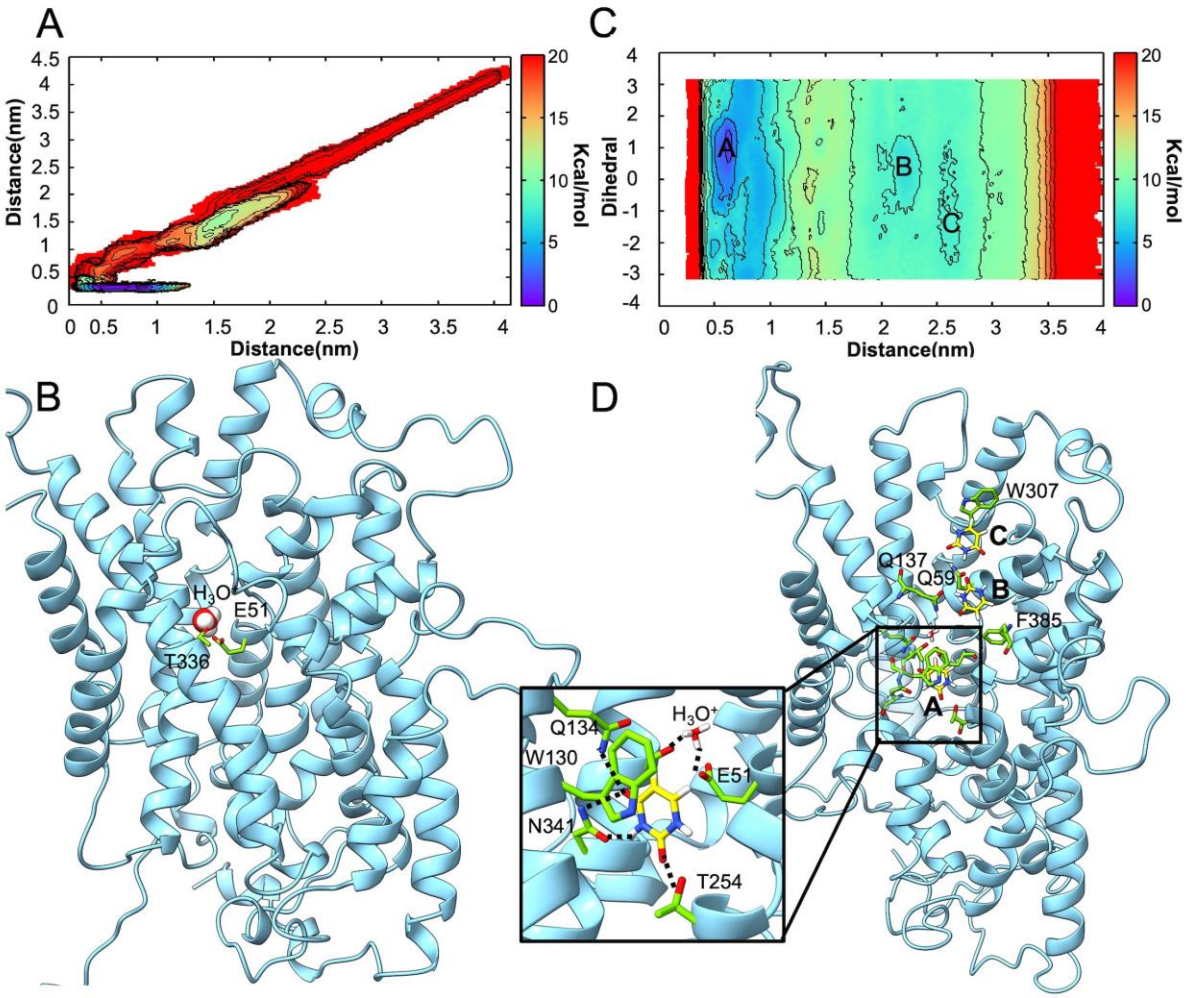

Figure 3: The binding site of H_3O^+ and uracil along with other important low energy states. (A) The BFES of H_3O^+ binding process. Contour lines are shown every 2 kcal/mol. (B) The binding mode of H_3O^+ cation in FurE transporter as derived from the global energy minimum in the FES. (C) The BFES of uracil binding process in FurE transporter. (D) The intermediate states (local minima in the BFES) of uracil entering FurE transporter and the binding mode in the binding site (inset) as derived from the BFES in C.

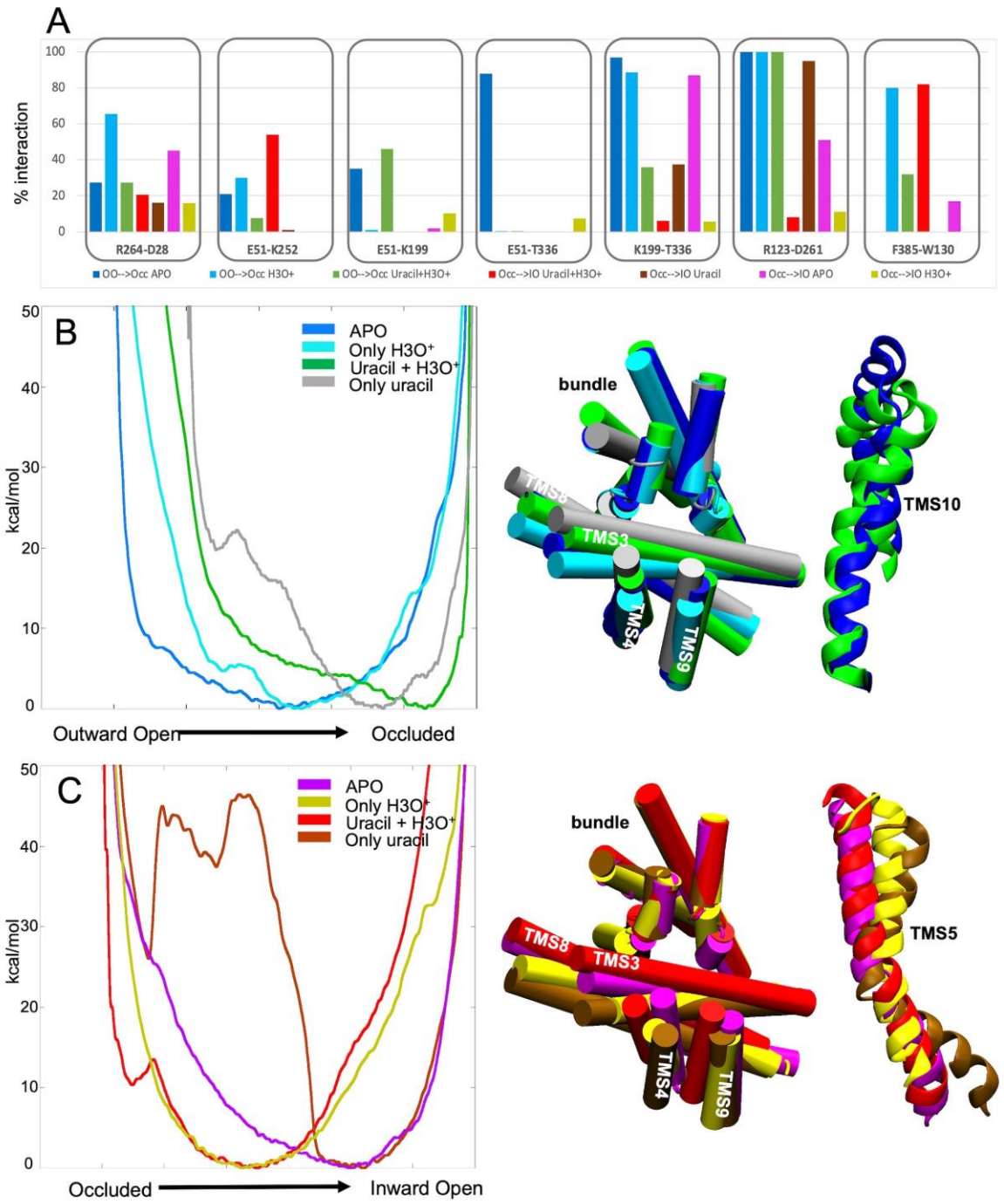

Figure 4. FurE conformational change and mechanism of transport. (A) The side chain interactions of important residues have been monitored in all structures collected in each FES global minimum and are represented as percentage over the ensemble of the structures. (B) The FESs of the OO-to-Occ transition using different stoichiometry of ligands bound to the transporter (colour code: protein in the *apo* form in blue, complexed only with H_3O^+ in cyan, complexed with both uracil and H_3O^+ in green, complex only with uracil in grey. Each tick in the x axis represents one unit. (C) The FESs of the Occ-to-IO transition are shown using different stoichiometry of ligands bound to the transporter. The system containing both uracil and H_3O^+ is represented in red, the system containing only uracil Is represented in brown, the *apo* form is represented in magenta, the system containing only H_3O^+ is represented in yellow.

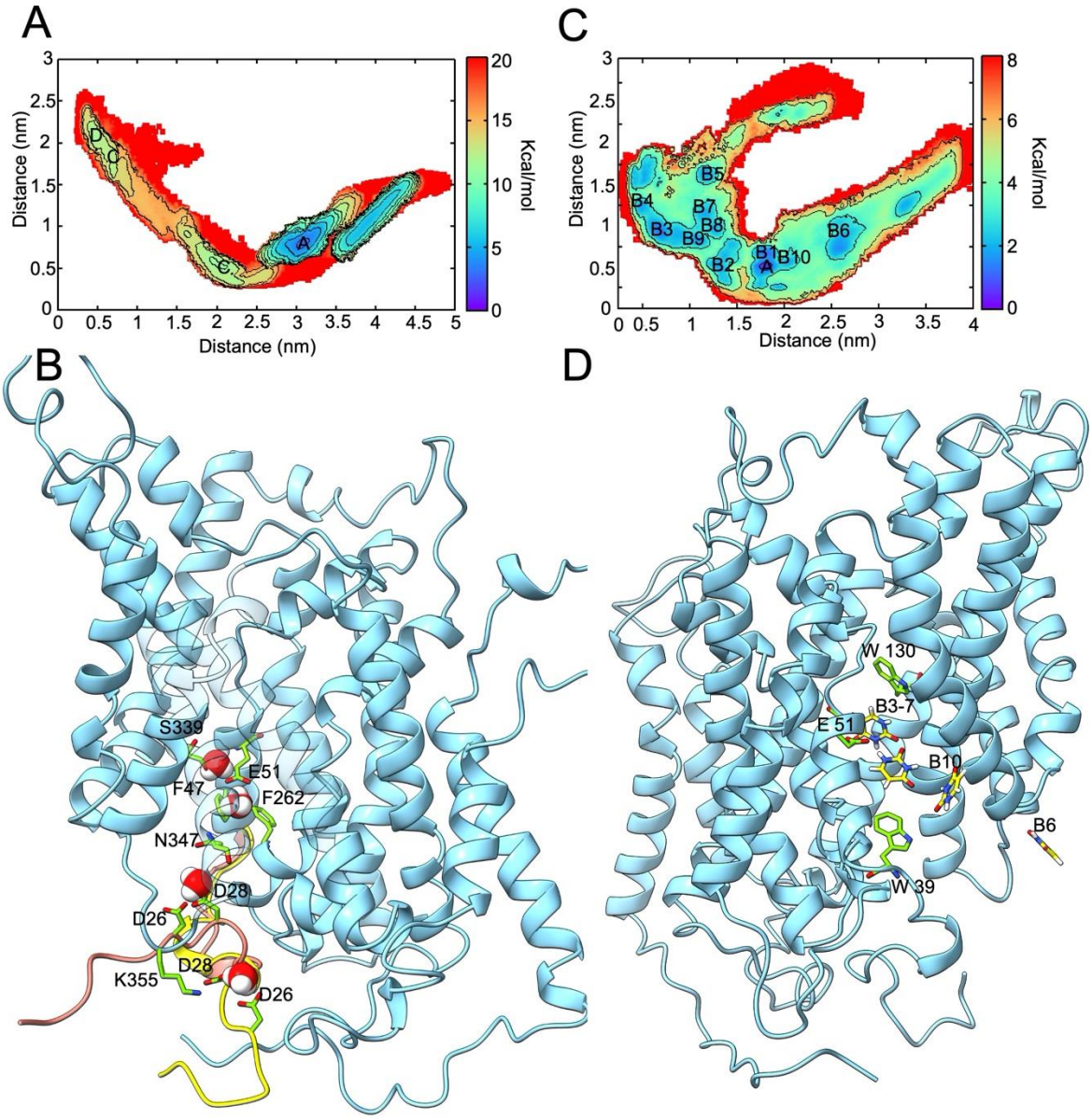

Figure 5. The unbinding process of H_3O^+ and uracil that characterize the exiting route to the cytoplasm. (A) The BFES of H_3O^+ internalization process. The separation between contours is 2 kcal/mol. (B) The binding sites of H_3O^+ cation in FurE transporter allong the internalization pathway as derived from the low energy states in the BFES in A. In orange is represented the LID when H_3O^+ is bound in D26, D28 and N347, while in yellow when H_3O^+ is released in the cytoplasm guided by D26, D28 and LID conformational change. (C) The BFES of uracil internalization process. The separation between contours is 2 kcal/mol. (D) The intermediate states of uracil internalization pathway while exiting FurE transporter as derived from the BFES in C.

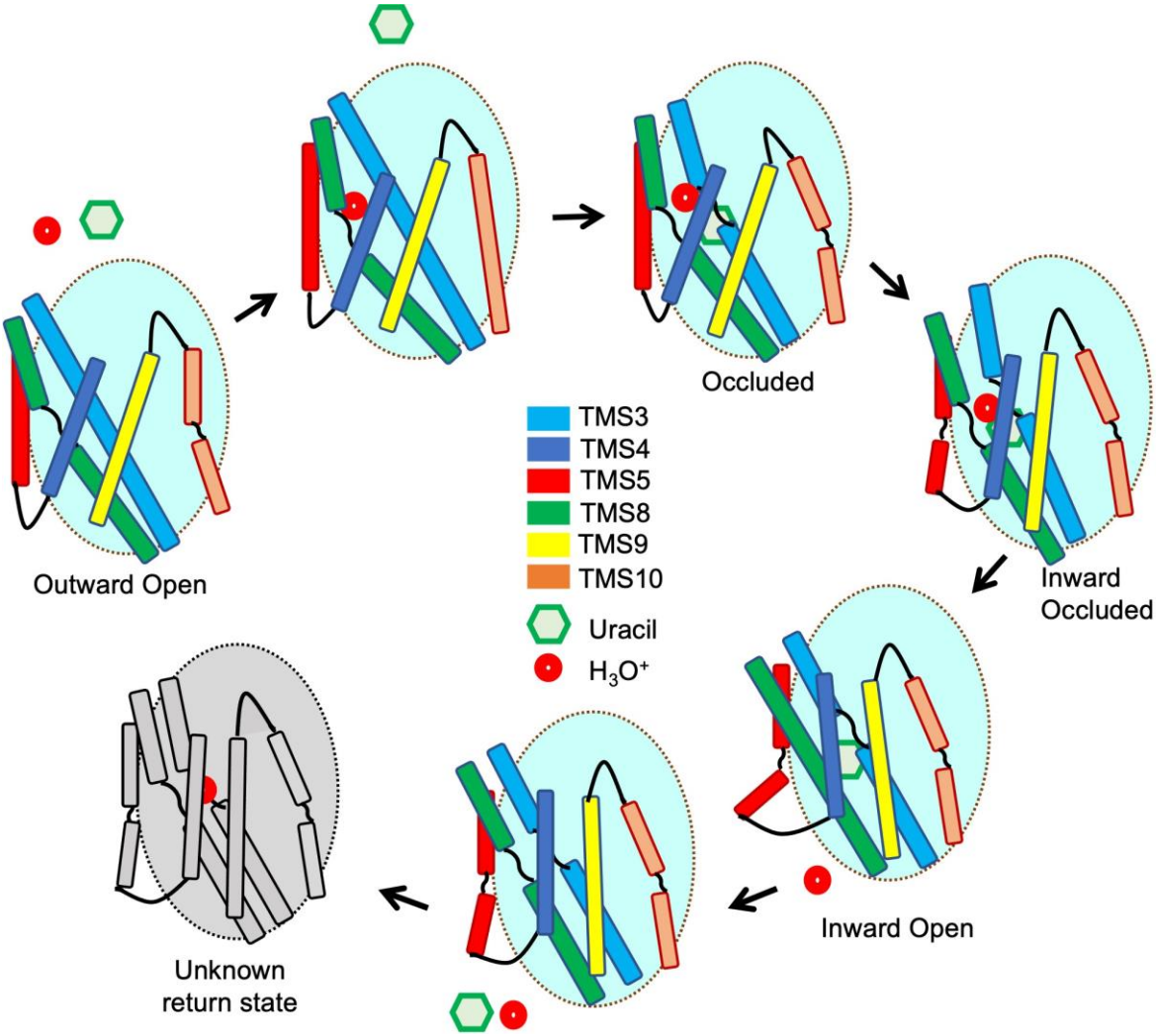

Figure 6: Schematic representation of the FurE's "hash" motif helices and outer and inner gates (TMS10 and TMS5) relative to the bundle motif which is considered immobile during uracil and H_3O^+ internalization. In the Outward Open (OO) state, FurE is in *apo* form. H_3O^+ binding results in residue rearrangement but it does not cause any rearrangement in the tertiary structure. Uracil binding induces the closing of theTMS10 outer gate (salmon) and the kink and tilt of TMS8 (green) and TMS3 (cyan), respectively reaching the Occluded (Occ) state. H_3O^+ moves toward the TMS5 inner gate (red), which slightly bends, while TMS3 and TMS8 also display structural rearrangements, initiating the Inward Occluded (IOcc) state. After H_3O^+ is released in the intracellular space, TMS5 bends more, while TMS8 is not tilted anymore moving away from the "bundle". TMS4 and TMS9 are shifted by TMS5, 8 and 3 bending introducing the Inward Open (IO) conformation. After the release of both H_3O^+ and uracil, TMS5 slightly returns to the previous bend position. An inward-facing unknown return state probably introduced by a H_3O^+, is represented in grey.

SUPPLEMENTARY MATERIAL

Table S1: The simulation time of each case of the PCV Metadynamics simulations.

Op-to-Occ	*apo*	H_3O^+	H_3O^+ +uracil	uracil
Time(ns)	352	550	600	430
Occ-to-In	*apo*	H_3O^+	H_3O^+ +uracil	uracil
Time(ns)	330	390	314	298

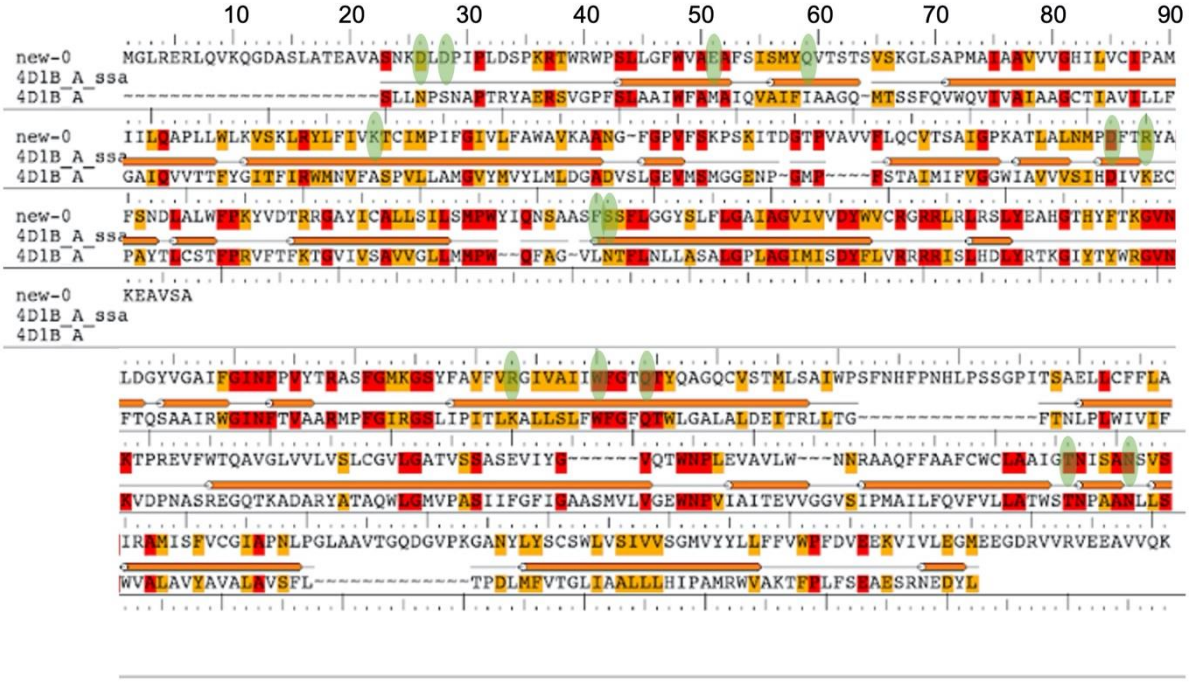

Figure S1: Alignment of FurE and Mhp1 (PDB ID 4D1B). Important residues studied in this work are highlighted in green.

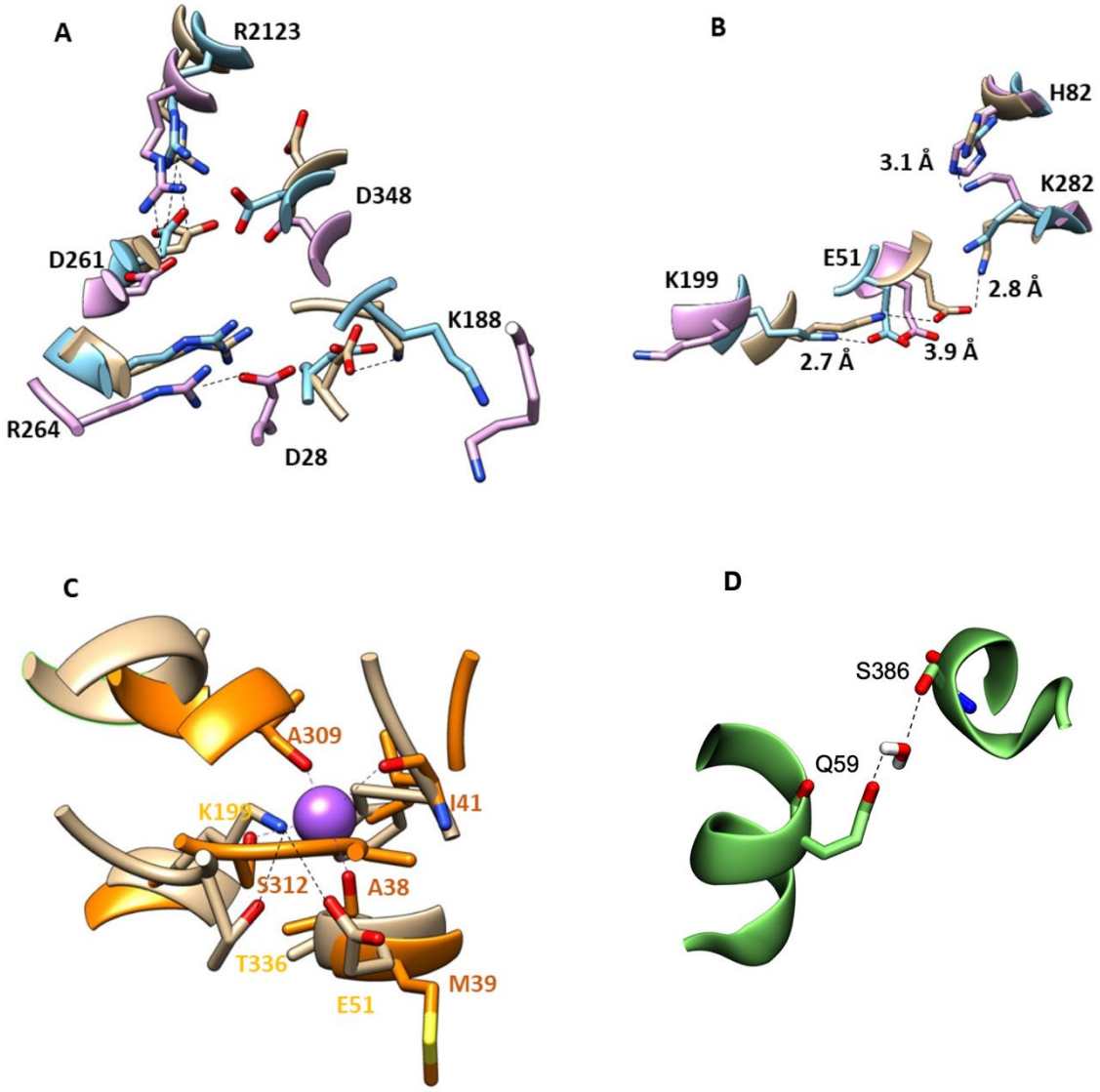

Figure S2. Details of interactions between residues in FurE models. (**A**) Interactions between D261-R123 (and vicinity with D348), R264-D28 and D28-K188 shown with black dashed lines and compared in the three FurE conformers (color code: OO in chaki, Occ in cyan, IO in pink). (**B**) Interaction between K199 and E51 in the different FurE conformers are shown in black dashed lines along with distances in Å (color code as in A). **(C)** In Outward Open (OO) conformation the interaction between K199-E51-T336 in FurE model (in chaki) is shown with black dashed lines. When compared with the corresponding cavity of Mhp1 (superimposed in orange), the FurE K199 amino group is located in the same position as the co-crystalized sodium (in magenta) in Mhp1 structure. Mhp1 sodium is coordinated by the S312 and T311 side chains along with A38, I41 and A309 backbone oxygens (magenta dashed lines). (**D**) Interaction between Q59 and S386 through a water molecule in FurE model MD simulation.

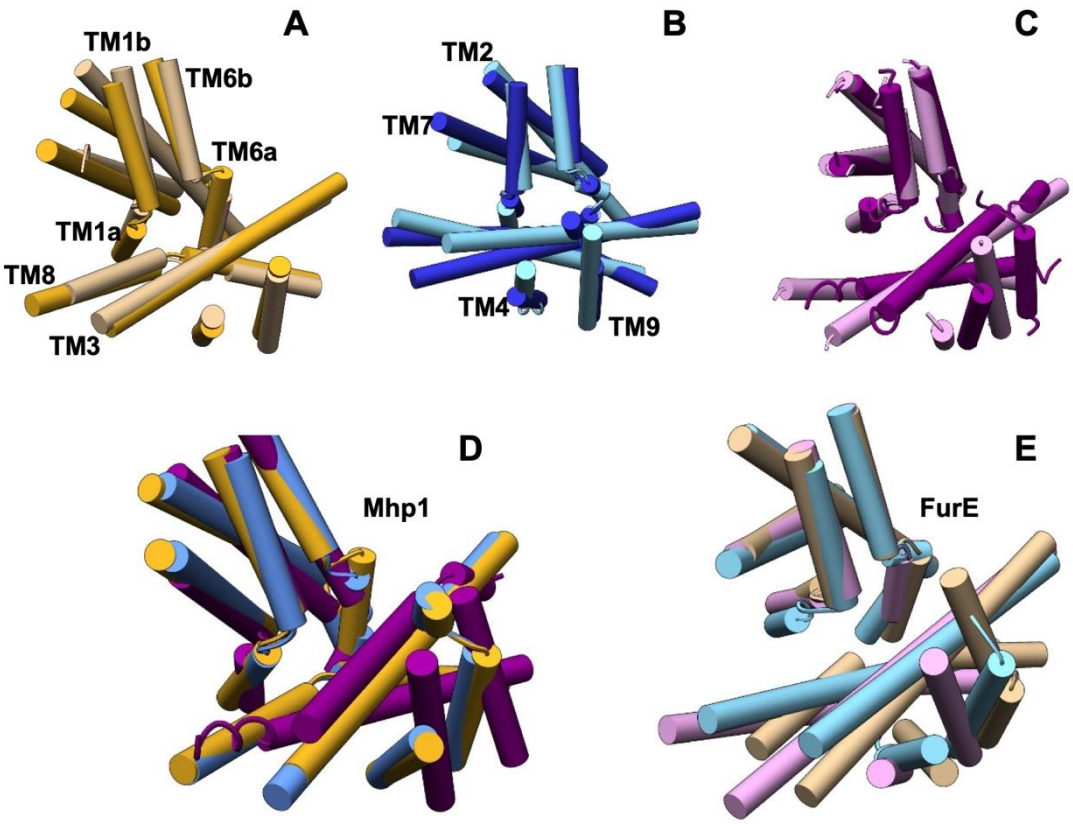

Figure S3. Relative orientation of transmembrane helices of the "hash motif" (TM3, 4, 8, 9) compared to the "bundle" (TM1, 2, 6, 7) in both Mhp1 template crystal structures and the homology models of FurE as resulted after a 50 ns MD relaxation. All structures are aligned on the "bundle motif" and are shown as cylinders for better resolution. (A) Comparison between OO structures of Mhp1 (gold) and FurE (yellow). No major differences are observed. (B) Comparison between Occ structures of Mhp1 (blue) and FurE (cyan). Small difference in TM3 is observed. (C) Comparison between IO structures of Mhp1 (magenta) and FurE (pink). Differences in the orientation of TM4 and TM9 are observed. (D) Superimposition of the three structures of Mhp1 OO (gold), Occ (blue), IO (magenta). (E) Superimposition of the three structures of FurE OO (khaki), Occ (cyan), IO (pink).

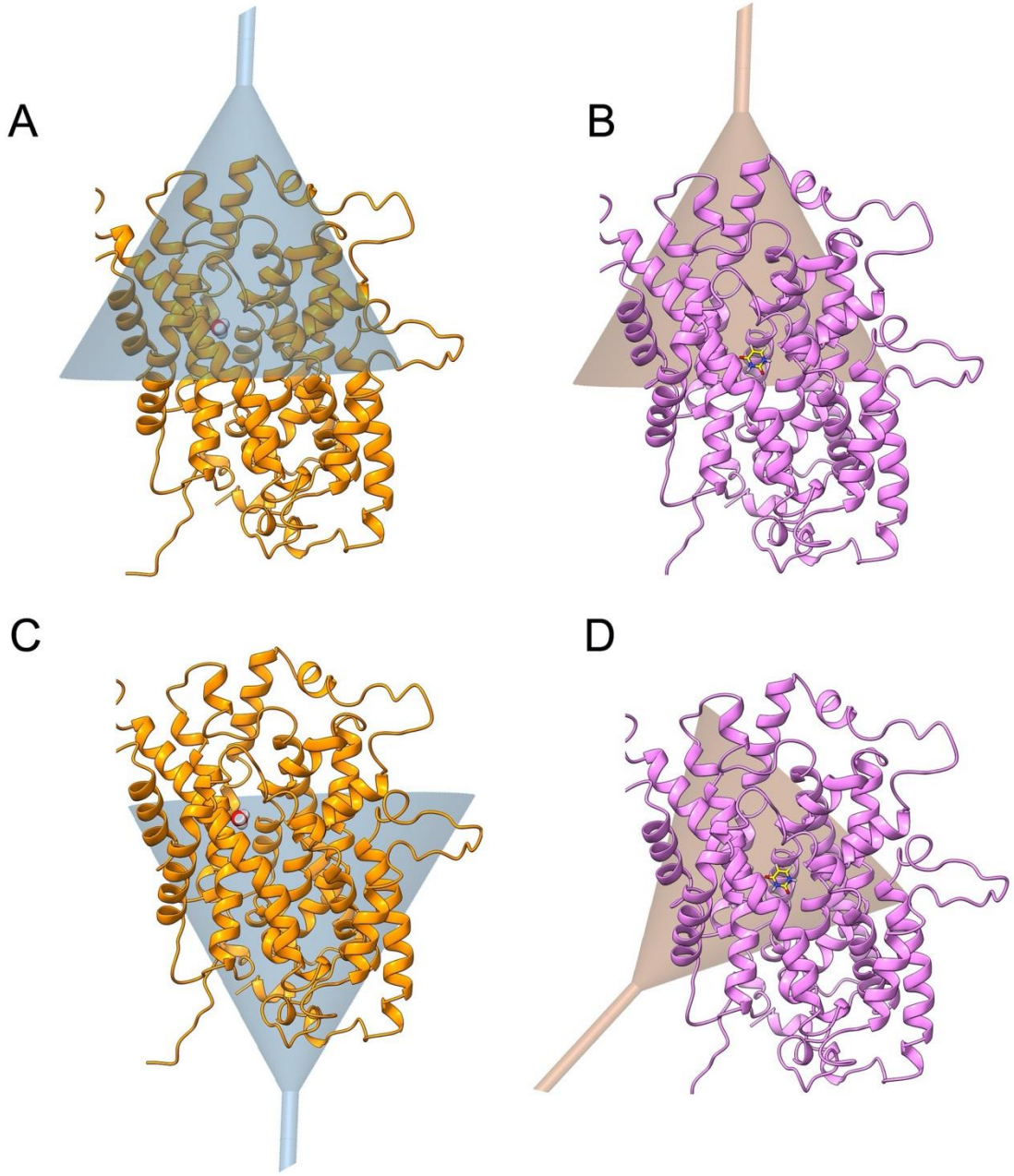

Figure S4: Funnel dimensions used for the four cases of FM simulations: (**A**) the funnel investigating the entrance of H_3O^+ in FurE transporter. (**B**) The funnel investigating the entrance of uracil in FurE transporter. (**C**) The funnel investigating the internalization process of H_3O^+in FurE transporter. (**D**) The funnel investigating the internalization process of uracil in FurE transporter.

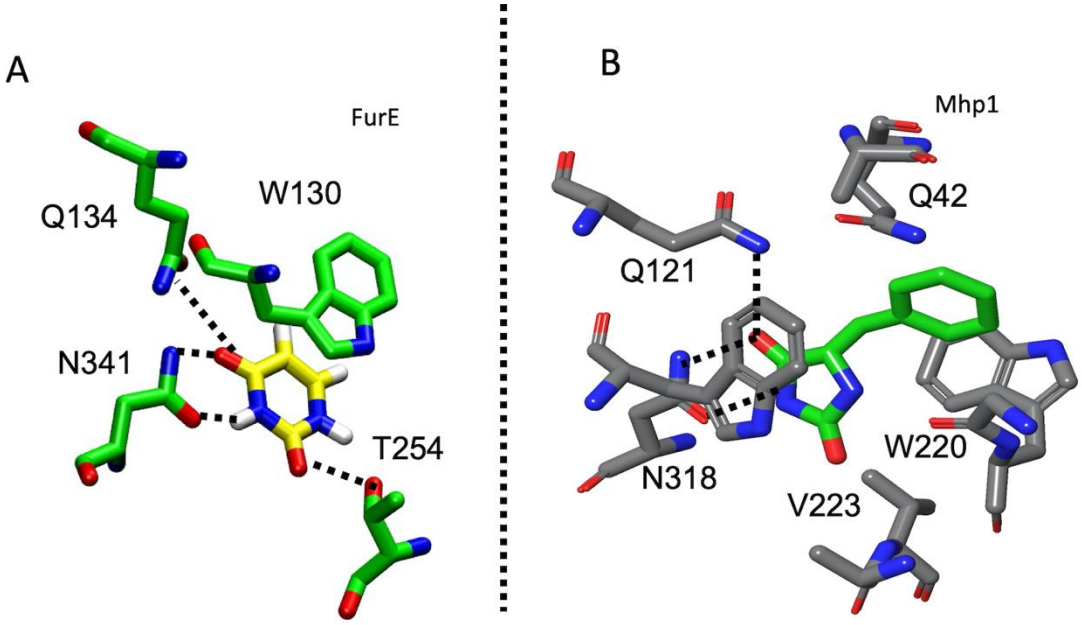

Figure S5: Comparison of the binding mode of (**A**) uracil in FurE with (**B**) (5S)-5-benzylimidazolidine-2,4-dione in Mhp1.

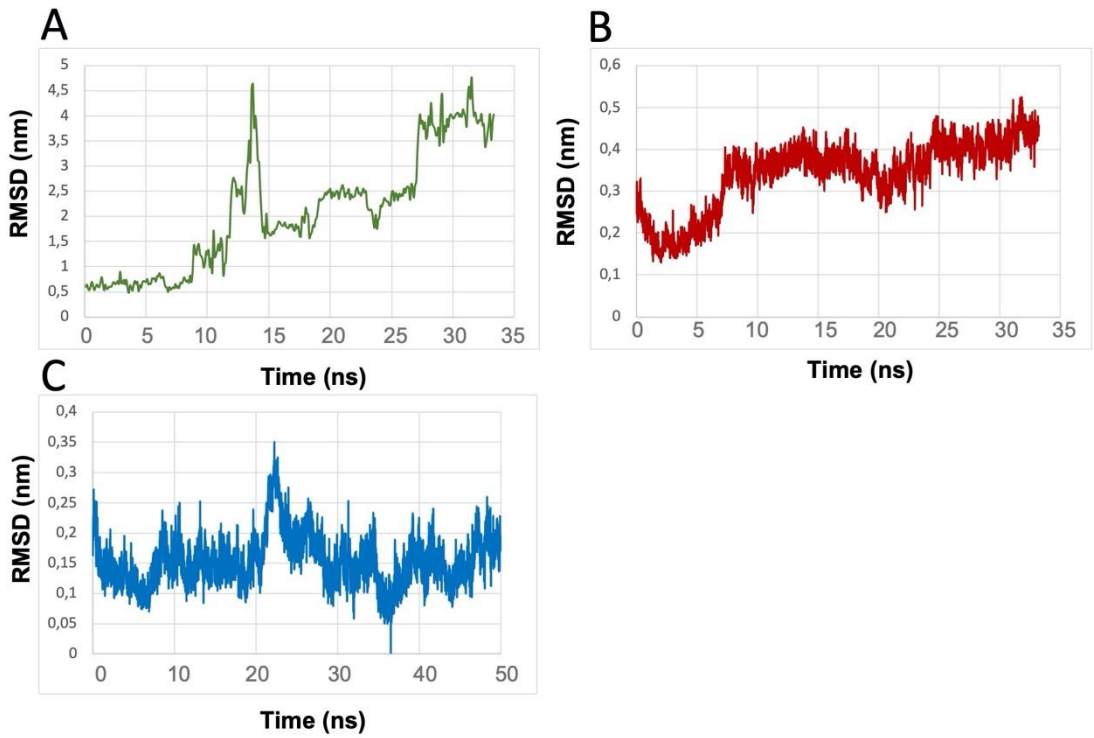

Figure S6: RMSD diagrams. (**A**) The RMSD fluctuation of uracil during an unbiased Molecular Dynamics simulation in the occluded FurE structure until it is out of the transporter, with uracil included and H_3O^+ not included. (**B**) The RMSD fluctuation of TMS10 during an unbiased Molecular Dynamics simulation in the occluded FurE structure, with uracil included and H_3O^+ not included. (**C**) The RMSD fluctuation of TMS10 during an unbiased Molecular Dynamics simulation in the outward *apo* FurE structure.

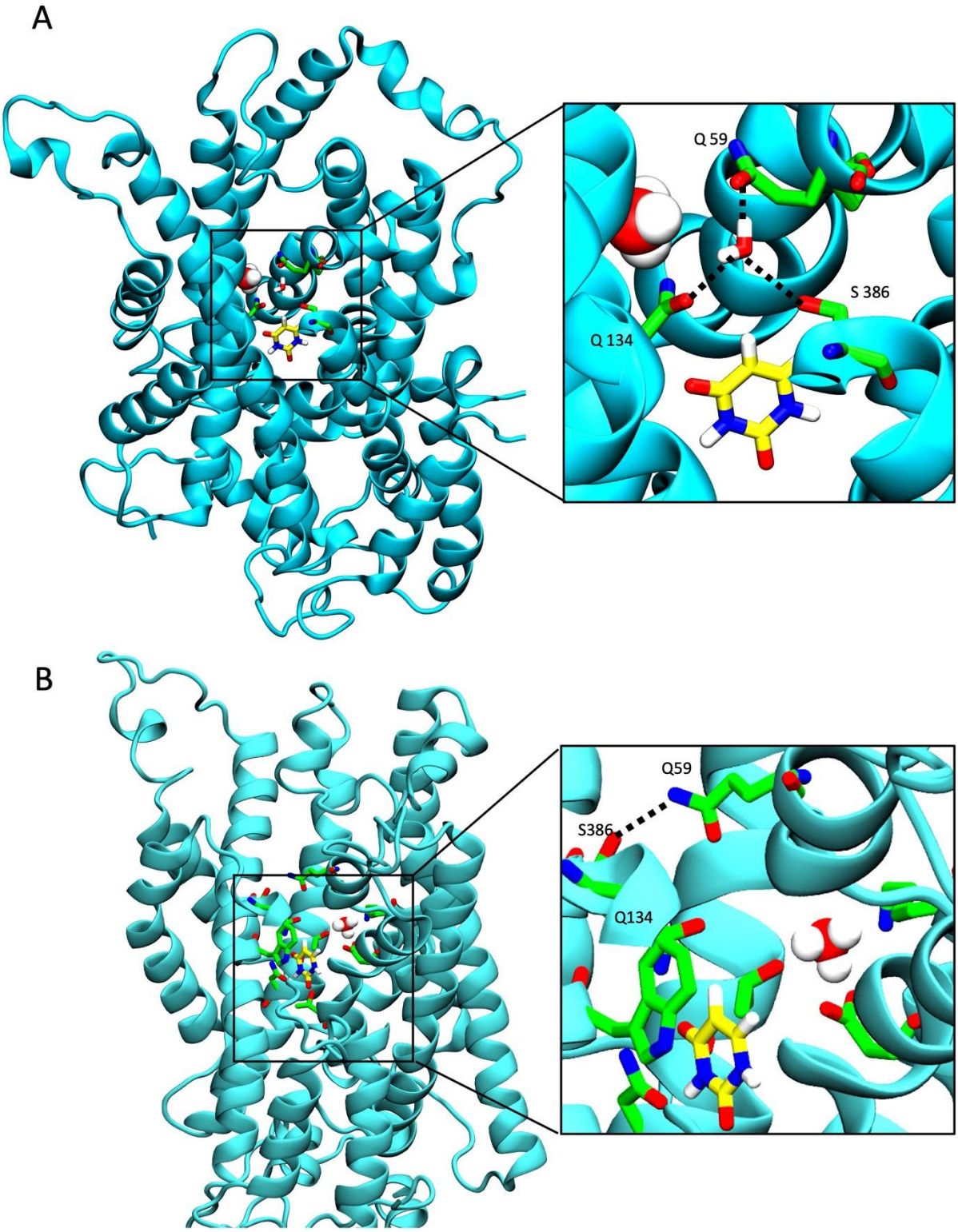

Figure S7: S386-Q59 interaction stabilize the Occ conformation of FurE by closing the TMS10 outer gate. (**A**) S386 interacts with Q59 through an H-bond network which involves a water molecule. (**B**) S386 forms a direct H-bond with Q59.

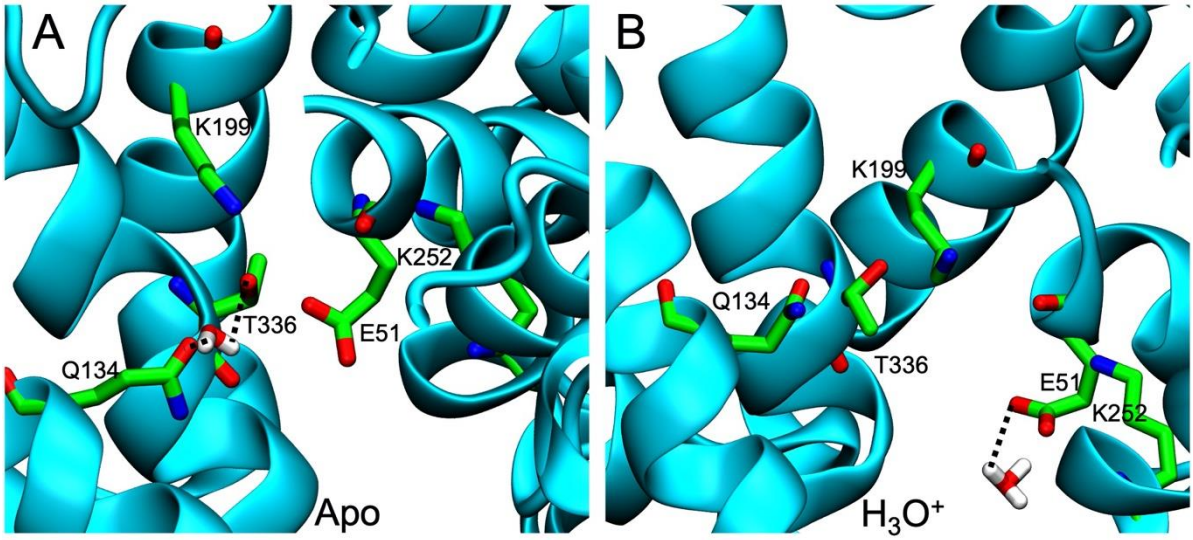

Figure S8: Different residue interactions in the absence and presence of $H3O^+$ cation in the OO FurE conformation. (**A**) When FurE is in APO Form, E51 interacts strongly with K199 and less often with K252. The orientation of T336 oxygen is towards TMS3 as T336 interacts with Q134 through H-bond network involving a water molecule. (**B**) When $H3O^+$ is present the electrostatic bond between K199 and E51 is less likely to happen, while is more likely for K252 to interact with E51. T336 side chain has also rotated by 180 degrees as it interacts with $H3O^+$ as displayed in Figure 1B. When $H3O^+$ is present T336 side chain oxygen is directed towards TMS5, thus the interaction with Q134 is broken and the latter is free to bind the substrate (uracil).